

Determination of the Influence of Stress, Time and Bedding Orientation on the Evolution of Contact Area and Stress Distribution for Fractures in the Opalinus Clay Shale

Written by:

O.M.G. Janssen

4110854

MSc Thesis

Period: September 2020 – May 2021

Supervisors:

Dr. Suzanne J.T. Hangx

*Utrecht University, High Pressure and Temperature Laboratory, Department of Earth Sciences
First supervisor*

Dr. Miao Zhang

*Utrecht University, High Pressure and Temperature Laboratory, Department of Earth Sciences
Second supervisor*



1. Abstract

Humanity is facing one of the largest challenges it has come up against in its lifetime, climate change. Emission of greenhouse gasses being the largest contributor to global warming, we need to change our way of living, producing energy and transporting products all over the planet. Emission of greenhouse gasses needs to be kept at a minimum and social change only will probably not be enough. On the short term the so called techno-fixes, where technology comes in play, can help us taking a step towards reaching our mutual goal of reducing CO₂ emissions. One of the most promising techno-fixes in play is Carbon Capture Storage (CCS) where CO₂ is captured at the source and is geologically stored in empty reservoirs or aquifers where it can be contained for geological timescales. Of course, the storage of CO₂ comes with certain risks as parts of this method are still unknown, such as the leakage potential of the in situ caprock. In this study the aim was to obtain empirical relationships for contact area and stress distribution with varying bedding orientation, stress and time for fractures in clayey caprock, in this case the Opalinus Clay shale. By performing compressibility tests with varying bedding orientations, stress and time, using pressure sensitive paper with different stress thresholds, it was observed that; 1. Intact compressibility tests show an increasing matrix compressibility with decreasing bedding orientation; 2. The effect of bedding orientation on the evolution of free space area and >15 MPa-bearing contact area with increasing applied stress shows to be neglectable and therefore empirical relationships were obtained regardless of bedding orientation; 3. Joint Roughness Coefficient (JRC) shows increasing trend with increasing bedding orientation angle ($0^\circ < \theta < 90^\circ$); 4. The effect of time is visible in a logarithmic trend, where applied normal stress plays a ~1:1 role; 5. The effect of an applied initial dislocation along the fracture plane shows an increase in contact area with increasing time, which implies there is a strong self-healing property present in the Opalinus Clay shale.

Table of Contents

1. Abstract	2
2. Introduction.....	4
3. Methods	5
3.1. Sample material.....	5
3.2. Experimental methods	6
3.2.1. Intact compressibility test	6
3.2.2. Brazilian splitting test	7
3.2.3. Compression tests of fractured shales	8
4. Results	10
4.1. Stress cycling data on intact samples (calibration of intact matrix compressibility)	10
4.2. Tensile strength and fracture toughness	11
4.3. Results of compression tests of fractured samples.....	12
4.3.1. Results of multiple-stress-steps tests on fractured samples of different bedding angle ...	13
4.3.2. Results of creep tests: Effect of time & fracture offset.....	17
5. Discussion	23
5.1. Intact compressibility experiments	23
5.2. Comparison of tensile strength and fracture toughness with previous research.....	24
5.3. Compression of fractured shales.....	25
5.3.1. Effect of bedding orientation	25
5.3.2. Effect of time & offset	28
6. Conclusions.....	32
Acknowledgement.....	33
References.....	33
Appendix A	35
Appendix B	37
Appendix C.....	43

2. Introduction

In a time where the climate changes, renewable energies are a high priority and carbon emissions are required to be kept at a minimum. The world still highly depends on the use of fossil fuels for energy generation, and techniques like Carbon Capture Storage (CCS) [Herzog & Golomb, 2004] are considered to be of high importance to reduce global carbon emissions. Such technology involves capturing carbon dioxide (CO₂) before it reaches the atmosphere, at locations where emissions are high, and then storing it in depleted hydrocarbon reservoirs or deep saline aquifers. Technology and knowhow related to CCS has already much advanced through projects in the Netherlands like Porthos and Athos [Hack et al., 2019]. However, to ensure safe, long-term storage of CO₂ in the subsurface, leakage of the injected CO₂ from the storage location needs to be prevented. The leakage of CO₂ from geological storage sites can have a significant impact on the environment, e.g. on surface vegetation and subsurface microbial communities [Morales & Holben, 2014], and might therefore also have an economic impact [Harvey et al., 2013; Celia & Bachu, 2003].

When storing CO₂ in geological storage sites it is hard, if not impossible, to avoid any form of leakage. Due to the large variety of leak paths and unknown parts of the mechanical and hydraulic influence of injected fluids/gasses to the subsurface it is almost impossible to guarantee a system of zero leakage [Celia & Bachu, 2003]. The most common leak path is found along the borehole. When the sealing layer of cement does not fit the borehole correctly, these gaps will form potential leak paths for the injected CO₂ fairly close to the injection point and therefore this will be a geologically quick way for the CO₂ to migrate out of the storage site [Watson & Bachu 2009; Wigand et al., 2009; Celia & Bachu, 2003]. The CO₂ can also leak along more geological pathways. Several forms of migration of CO₂ can be observed in these systems. Vertical migration, which is faster due to the buoyancy force of the lighter CO₂ supercritical fluid, and lateral migration which is slower due to the lack of influence of the buoyancy force. For lateral migration the capillary pressure of pore throats is harder to overcome and therefore it takes more time for CO₂ to migrate in a lateral way [Celia & Bachu, 2003]. Both vertical and lateral migration out of the storage system can take place along different paths, such as through the caprock matrix and fractures in the caprock [Hou et al., 2012; Pyrak-Nolte et al., 1988; Neuzil & Tracy, 1981; Tsang, 1984].

As fracture permeability is typically several orders of magnitude higher than the matrix permeability of a shale, the fracture will be the main geological contributor to the potential leakage. Fracture permeability is controlled by some characteristic factors like connectivity, contact area and aperture width [Tsang, 1984; Brace, 1978]. As stated by Tsang (1984), the fluid flow through a fracture decreases with increasing normal stress owing to two factors: (1) Fracture apertures for fractures under increasing stress are smaller due to fracture closure with stress. (2) There is an increase in tortuosity and a decrease in connectivity of fluid flow paths due to an increase in contact area with time. Therefore it is of importance to investigate how these characteristics evolve under stresses relevant to storage conditions to better understand fracture permeability.

In the present study, samples cored from the Opalinus shale were investigated, as this is a typical and well-characterized [Bossart & Thury, 2008] clay-rich rock and clayey rocks are common caprocks for e.g. CO₂ storage systems. Single fracture with the fracture plane having an angle of 0-90 degree to the bedding orientation of the sample was derived in each sample using Brazilian splitting method, the tensile strength and fracture toughness of the OPA material were determined. Besides, the fracture roughness versus fracture orientation was explored. Two types of uniaxial compression tests were then performed on the fractured samples, i.e. (1) stress cycling tests performed at multiple stress steps

in the range of 0.5-15MPa and (2) creep tests performed with constant stress acting on the fracture plane. The evolution of characteristic parameters (connectivity, contact area and aperture width) of the fractures with different orientations as a function of normal stress. Both types of tests were performed with pressure sensitive sheet (PSP), which is a thin film which indicates pressure distribution and pressure magnitude between two surfaces in contact, in-between the two sides of the fracture. Force versus displacement data obtained in test (1), also performed without PSP, allows evolution of fracture aperture under the effect of stress, stress history (time-dependent behaviour) to be characterized after calibrating matrix deformation using compression tests on intact samples. On the other hand, evolution of fracture contact under the effect of stress, stress history (time-dependent behaviour) and bedding orientation were investigated via tests using PSP. Two questions would be answered through this research: (1) What will be the influence of different normal stresses on the evolution of stress distribution and contact area along the fracture plane? (2) What will be the influence of time on the evolution of stress distribution and contact area along the fracture plane? These questions will be answered on the basis of the experiments that will be performed during this study. Intact compressibility test will be performed where matrix deformation will be measured in order to distinct matrix compaction from fracture compaction in the fractured shale compressibility tests.

Empirical relationships describing the fracture roughness evolution, and hence fracture aperture, as a function of time and stress are derived, which can be further used in numerical models for a first-order assessment of the leakage potential of fractures in clayey caprock under different storage conditions.

3. Methods

3.1. Sample material

The Opalinus Clay (OPA) has been deposited approximately 180 million years ago during the Middle Jurassic as a part of the Liassic-Dogger units, which contains several shallowing-upward regressive cycles and ending with shallow-water carbonates [Bossart & Thury, 2008; Bossart et al., 2017]. The Opalinus Clay, as a lithostratigraphic formation, consists of sequence of dark grey, silty micaceous clays and sandy shales. Therefore, it is classified into three facies in terms of the enrichment of quartz, carbonates and silts, namely sandy facies, carbonate rich sandy facies and shaly facies [Bossart et al., 2017]. The source material used in our present research are shaly-facies cores drilled at Mont Terri Underground Rock Laboratory (URL), which is typically composed of 50-65% clay particles, consisting mostly of kaolinite and illite while the other ~35% consists of quartz, calcite and feldspar minerals (Table 1). [Corkum et al., 2007]

Table 1 - Mineral composition of Opalinus clay according to Corkum et al. 2007.

Mineral	%	Mineral	%
Kaolinite	30	Quartz	20
Illite	17	Calcite	7
Illite-smectite	10	Feldspar	3
(mixed layers)		Siderite	2
Chlorite	8	Dolomite/ankerite	1
		Pyrite	1
		Organic carbon	0.4
Total clay	65	Total non-clay	35

The source OPA cores were sleeved using aluminium foil after being drilled at URL to prevent water loss and weathering. Cylindrical samples with diameter of ~25mm and varying lengths were plugged from the source material. The samples can be divided into two types based on the bedding orientation relative to the longitudinal axis of the sample, namely bedding parallel samples (i.e. with long axis of the sample parallel to bedding) and bedding perpendicular samples (having its bedding perpendicular to the axis of the sample). In order to keep as close to the original water content as possible (roughly 8-9 vol.%, *Bossart et al., 2017*), the samples were wrapped in bubble wrap and stored in individual airtight containers, with the containers placed in environment buffered by synthetic brine (i.e. Pearson's brine, *Pearson et al. 2003*). The characteristics of the used samples are shown in Appendix A.

3.2. Experimental methods

The experimental workflow adopted in the present study consist of three main steps, with each step having their own purpose, explained below:

1. **Compression tests on intact samples :** Uniaxial stress cycling were done in these tests to get the compression data, i.e. force (F) versus displacement (L), for intact samples of different bedding orientations. Also, whether deformation of the intact sample is reversible was verified. Note that the displacement measured (ΔL) consists of the deformation of the matrix of the sample and the deformation of the apparatus used during this experiment. Such data (ΔL versus ΔF) is needed in order to distinct the fracture deformation from the deformation of the whole (fractured) sample. Besides, the compaction of the intact samples with different bedding orientations will show the influence of bedding orientation on the compressibility of the Opalinus clay.
2. **Brazilian splitting test:** This is aimed to create fractured samples containing a single fracture of different orientation relative to the bedding. Most samples studied in this research were fractured using a Brazilian splitting rig illustrated in figure 2, while four samples were fractured using a different method described by ISRM (1978) in order to determine the tensile strength and the fracture toughness (Figure 3).
3. **Compression tests of fractured shales with and without pressure sensitive paper (PSP):** The compaction of fractured samples is combined with the usage of PSP's in order to visualize the contact area and to determine the stress distribution along the fracture plane. The results of this set of experiments will indicate the influence of various normal stresses and time on the evolution of the contact area and its stress distribution. There are three experiments performed without PSP in order to distinguish the fracture compaction for each applied normal stress.

3.2.1. Intact compressibility test

Experimental setup, sample assembly and procedure

As a preparation for future experiments, most used samples go through the intact compressibility tests. The sample will be fitted in a custom made semi-cylindrical sample holder as shown in figure 1. In order to fit the diameter to the 1 inch diameter of the sample holder, fitting spacers are used with varying thicknesses and materials (copper, steel). This is done so that the sample will not deform in an elliptical way. The maximum force exerted on the sample was determined to apply a stress perpendicular to the orientation of the fracture plane to be induced at the magnitude of 10 to 15 MPa. This stress is estimated based on the stress acting on the largest area (i.e. middle plane) of the sample.

Each sample undergoes three cycles of loading between ~ 0.2 MPa and the maximum stress. Displacement of the upper loading piston relative to the lower loading piston is recorded by a local LVDT in order to calculate the differences in diameter after each stress cycle. Appendix A shows the samples used for this set of experiments.

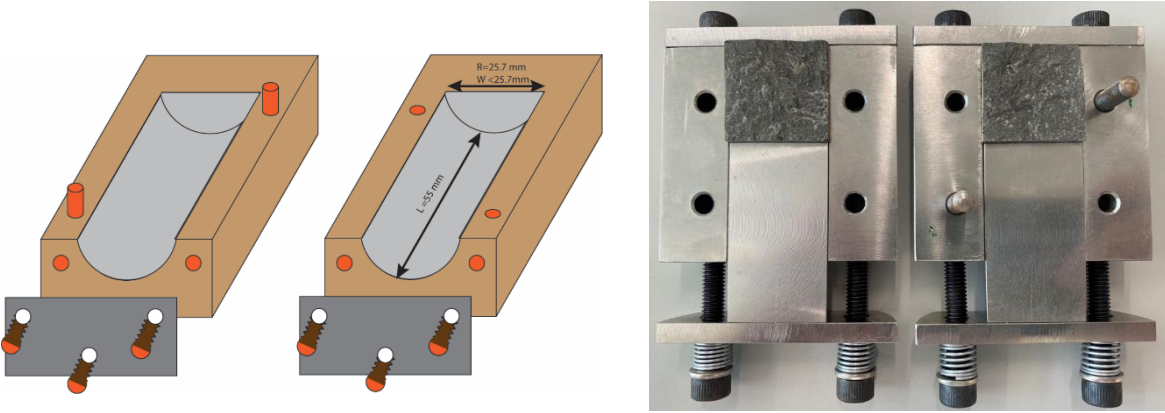


Figure 1 - Custom sample holder designed to accommodate the cylindrical sample and apply normal stress perpendicular to the orientation of the fracture plane generated (Left). It is also designed to fix upper and lower parts of the fractured sample and then align the two parts in uniaxial compression test on fractured sample (Right).

3.2.2. Brazilian splitting test

3.2.2.1. Experimental setup, sample assembly and procedure

Each sample was fractured using the custom Brazilian splitting apparatus (Figure 2). This method is different than is used in other studies. Instead of a flat surface or a cylindrical sample holder, there are two wedge shaped blades installed in the sample holder. The top part is able to move as stress is applied to the sample. The wedge-shaped blades will cut into the sample, eventually splitting the sample. The thickness and angle (sharpness) of the blades is of high priority as this contributes to the aperture width during fracturing. The angle of the blades is 19.5° . During the loading test, the Instron apparatus on which the sample holder is placed compresses the blades into the sample at a speed of 0.1 mm/min. Displacement of the upper loading piston relative to the lower loading piston is recorded by a local LVDT (Linear Variable Differential Transformer) installed adjacent to the sample, hence allowing sample deformation to be measured after correcting for deformation of the loading set-up. Signal of the position of the apparatus (mm), the applied load (kN) and the local LVDT values (mm) were logged at a rate of 30 Hz.

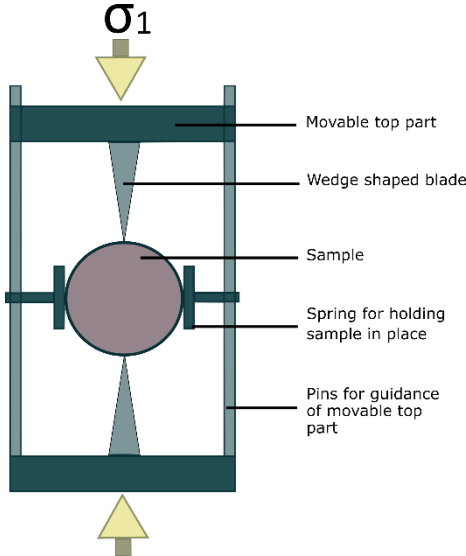


Figure 2 - Brazilian splitting setup

Before the sample was installed in the sample holder for the Brazilian splitting test, the sample needs to be prepared. Notches were made at the middle of the ends and two sides the sample. Notches at the ends are attempted to guide the induced fracture to propagate along the middle plane of the

sample, while the notches at the sides aimed to facilitate instalment and alignment of the sample between the blades of the Brazilian splitting rig. The depth of this notch is about ~1mm.

Besides of samples fractured using modified Brazilian method, a few samples are fractured following the method as suggested by ISRM (1978), using flat-cylindrical loading pistons to apply the compressive force (Figure 3). Such conventional Brazilian splitting test allows calculation of the tensile strength (MPa) and fracture toughness using formulas given by ISRM (1978) and Chandler et al. (2016).

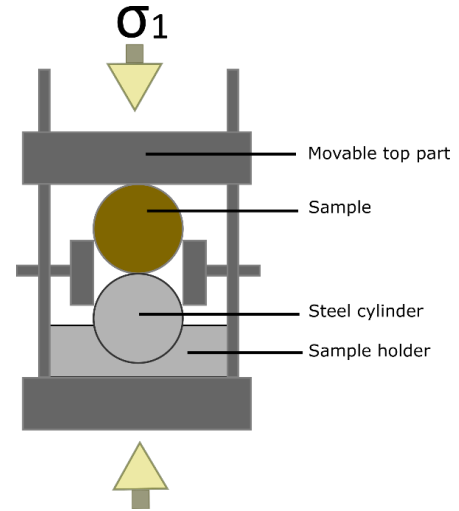


Figure 3 - Flat-cylindrical Brazilian splitting test setup used for calculating cohesive strength and fracture toughness.

3.2.2.2. Data processing

In order to calculate the tensile strength, formulas used by ISRM (1978) and Chandler et al. (2016) will also be used in this study:

$$\sigma_t = 0.636 * \frac{F_{max}}{D*t} \quad (1)$$

Where σ_t is the tensile strength (MPa), F_{max} is the maximum applied load (N), D is the diameter of the sample (mm) and t is the length of the sample (mm). By using formula (1), Chandler et al. (2016) determined a trend in the tensile strengths of different materials which can be used to calculate the accompanying fracture toughness for these samples, using the formula determined by Chandler et al. (2016):

$$\sigma_t = 6.76 * K_{Ic} \quad (2)$$

Where K_{Ic} is the critical stress intensity factor (fracture toughness, $MN/m^{1.5}$). Formulas (1) & (2) are used to calculate the tensile strength and the accompanying fracture toughness for the samples that were fractured using the flat-cylindrical Brazilian splitting test.

Due to the difficulty of fracturing samples along different orientations in respect to the bedding of the sample as described by [Chandler et al., 2016], few samples were fractured along the correct orientation as fractures can deflect up to angles of 90° towards bedding planes with lower fracture toughness. Therefore, it will not be possible to get the empirical relationships of tensile strength vs. bedding orientation and fracture toughness vs. bedding orientation.

3.2.3. Compression tests of fractured shales

3.2.3.1 Experimental setup, sample assembly and procedure

In order to determine the evolution of contact area, and therefore fracture roughness, between both planes of the fracture, experiments using pressure sensitive paper (PSP, Fuji film) are performed. The PSP can be considered as an indicator revealing the contact of two interacting surfaces. It consists of a polyethylene sheet containing colour-developing micro-capsules. When the stress between two contacting PSP areas increases in excess of a threshold value, the micro-capsules will burst, and the impacted area will be stained red, with the colour density being indicative of the stress magnitude. Three types of PSP's with different stress thresholds were used, namely LLW, LW and MS. The LLW PSP has a threshold of 0.5 to 2.5 MPa, the LW PSP has a threshold of 2.5 to 10.0 MPa and the MS PSP has a threshold of 10.0 to 50.0 MPa. By compression tests using these three different PSPs sequentially, a

stress distribution map for the fracture surface can be derived over stress range of 0.5-50.0 MPa, through combining the results of all three PSPs.

All samples tested in this section are fractured using the modified Brazilian splitting method, ideally, leading to a single through-going fracture along the axis of the sample, with a desired angle relative to the bedding orientations. After fracturing, each half of the fractured sample was fixed in the custom sample holder as used in the compression tests on intact sample (Figure 1) and then re-aligned. The sample assembly as a whole was subsequently installed in the Instron machine, three cycles of fast loading and unloading were performed on the fractured sample, at a loading rate of ~ 0.08 kN/s. The range of force employed are in line with the configuration of the intact compressibility test. Dataset obtained from these experiments basically indicate the fracture compaction at different applied stresses. The first set of experiments were performed on samples with different fracture orientations relative to bedding (0° , 15° , 30° , 56.3° , 60° , 90°).

After stress cycling, multiple stress steps were applied normal to the fracture plane with a PSP placed in-between the two halves of the sample, in order to distinguish the effect of normal stress on the contact area. Each sample underwent 6 different normal stresses of 0.5, 3.0, 5.0, 7.0, 10.0 and 15.0 MPa. For each stress step, all three types of PSP are used sequentially, with the target stress applied for at least 2 minutes in order to make a good imprint on the PSP. These tests yield 18 PSP prints per sample (3 PSPs x 6 stress step), which eventually lead to 6 stress distribution maps, one per applied normal stress.

In addition to PSP tests under varying stress steps, three samples were subjected creep tests using PSPs, i.e. compression test under a constant normal stress. These experiments were performed to investigate evolution of fracture contact area vs. time, in other words, to investigate the effect of creep on fracture closing. Specifications of these three experiments are as follows:

1. Sample V14-01: Constant applied stress of 15 MPa without initial dislocation.
2. Sample V3: Constant applied stress of 15 MPa including an initial dislocation of 1.5 mm.
3. Sample V2: Constant applied stress of 5 MPa including an initial dislocation of 1.5 mm.

All three samples have a 90° fracture-to-bedding orientation and experiments on all three samples are performed at similar timesteps. During the experiments, pressure sensitive paper was used. The target normal stress was first applied for a time span of 15 minutes, with the LLW PSP sandwiched between the two halves of the sample. After this timespan, the LLW PSP would be replaced by a new LW PSP, and the sample would be compressed at the same stress for 2 minutes, followed by a repeated test using MS PSP to replace LW PSP. After the tests using three different types of PSP at the first timestep, the experiments then proceed to the following timesteps, respectively 1 hour, 4 hours, 16 hours and 24 hours. For sample V2 it is also performed after 68 hours. By using all three PSP types at each timestep, PSP prints reflecting contact area and stress distribution along the fracture surface after subjecting to constant normal stress for increasing timespan were collected.

3.2.3.2 Data processing

Each experiment will result in a set of partly red stained pressure sensitive papers (Figure 4). These papers were digitised for further analysis by scanning them using a scanner at 1200 dots per inch (dpi). These scanned images are cropped and properly aligned manually using the image processing program Fiji ImageJ[®]. ImageJ can transform these cropped images into tables with results of RGB/3 values for each pixel. A Matlab[®] script was developed which reads these RGB/3 values for each pixel and quantifies the stress values corresponding to these RGB/3 values by referring to the standard colour

patches of varying stress intensities as provided by Fuji. This script returns a new table containing stress values of the same size as the input table with the RGB/3 values, i.e. yielding a stress distribution matrix with the same resolution of the scanned image of the PSP prints, equivalent to 1200 dpi. This stress matrix is again imported into ImageJ, transformed into a stress distribution map with a colour scaling and legend.



Figure 4 - Red stained pressure sensitive papers (PSPs). Examples from sample H60-2 at an applied stress of 7.0 MPa. PSP with high stress threshold (MS) on the left, medium threshold (LW) in the middle and low threshold (LLW) on the right.

4. Results

4.1. Stress cycling data on intact samples (calibration of intact matrix compressibility)

During the compressibility of intact samples, applied force and local LVDT (Linear Variable Differential Transformer) data is collected. This LVDT data shows the displacement of the apparatus during the experiments.

The uniaxial force measured in compression tests on intact samples were divided by the length of corresponding sample, such that making the forces versus compaction data for samples of different lengths comparable. The normalized force per length data are plotted versus compaction in figure 5A which are hard to follow or see trend in. Therefore, a linear fit is made to each set of data and replotted

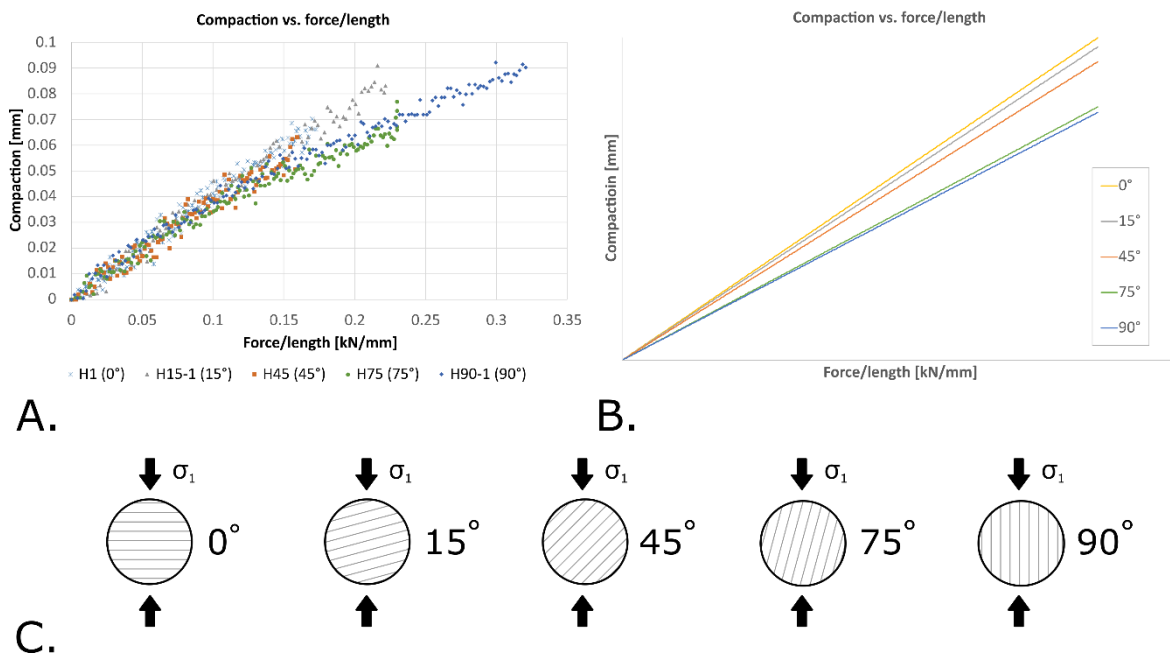


Figure 5 - A) Data points from intact compression experiments. B) Trendlines taken from experimental data. C) Illustrative explanation of used samples including angle.

in figure 5B that shows a more general trend. The slope of these trendlines represent the compressibility of each particular sample. Seeing from figure 5B, samples fractured parallel to the bedding (0°) have a higher compressibility while samples fractured at a high angle relative to the bedding (90°) attain a lower compressibility. In general compressibility is decreasing with increasing angle relative to the bedding. The compressibility values for each sample as derived from slope of each trendlines are summarized in table 2.

Note that the displacement measured contains not only the compaction of the sample, but also the compaction of the whole apparatus, sample holder and spacers used in each experiment. As all experiments were performed using the same set-up, this data can be used as a benchmark of the total deformation of the sample matrix plus the testing set-up, to distinguish the aperture deformation and change in aperture width in similar compression tests on fractured samples.

Table 2 - Compressibility of intact samples tested in compression experiments. The compressibility value is extracted from the slope of a linear fit to experimental data on displacement vs. force/length.

Sample	H1	H15-1	H45	H75	H90-1
Bedding Angle wrt loading direction (°)	0	15	45	75	90
Compressibility (mm²/kN)	0.3994	0.3881	0.3698	0.3138	0.307

4.2. Tensile strength and fracture toughness

The tensile strength (σ_t) and fracture toughness (K_{Ic}) of the four bedding-perpendicular Opalinus samples fractured using conventional Brazilian method was derived following *ISRM standard (1978)*, the main results are given in table 3.

Tensile strengths as well as fracture toughness give similar values for each sample. Overall trend shows that both tensile strength and fracture toughness decrease with increasing length. Only sample V17-03 differs from this trend, resulting in values, for both tensile strength and fracture toughness, that are lower than predicted by this rough trend.

Table 3 - Tensile strength and fracture toughness values, dimensions of used samples and maximum applied force.

Sample	Tensile strength [MPa]	Fracture toughness [MN/M^{1.5}]	Length (t) [mm]	Diameter (D) [mm]	Maximum applied force [kN]
V16-01	3.782	0.56	27.8	24.8	4.1
V17-01	4.004	0.59	11.4	24.8	1.78
V17-02	3.953	0.58	14	24.82	2.16
V17-03	3.532	0.52	20.4	24.8	2.81

4.3. Results of compression tests of fractured samples

Appendix B shows stress distribution maps for each sample used in this set of experiments, figure 6 shows an example of these stress distribution maps. Looking at the high stress bearing contact areas, this corresponds to the bedding plane sticking out of the fracture surface. This is clearly visible for each sample with a fracture-to-bedding angle (θ) higher than 0° .

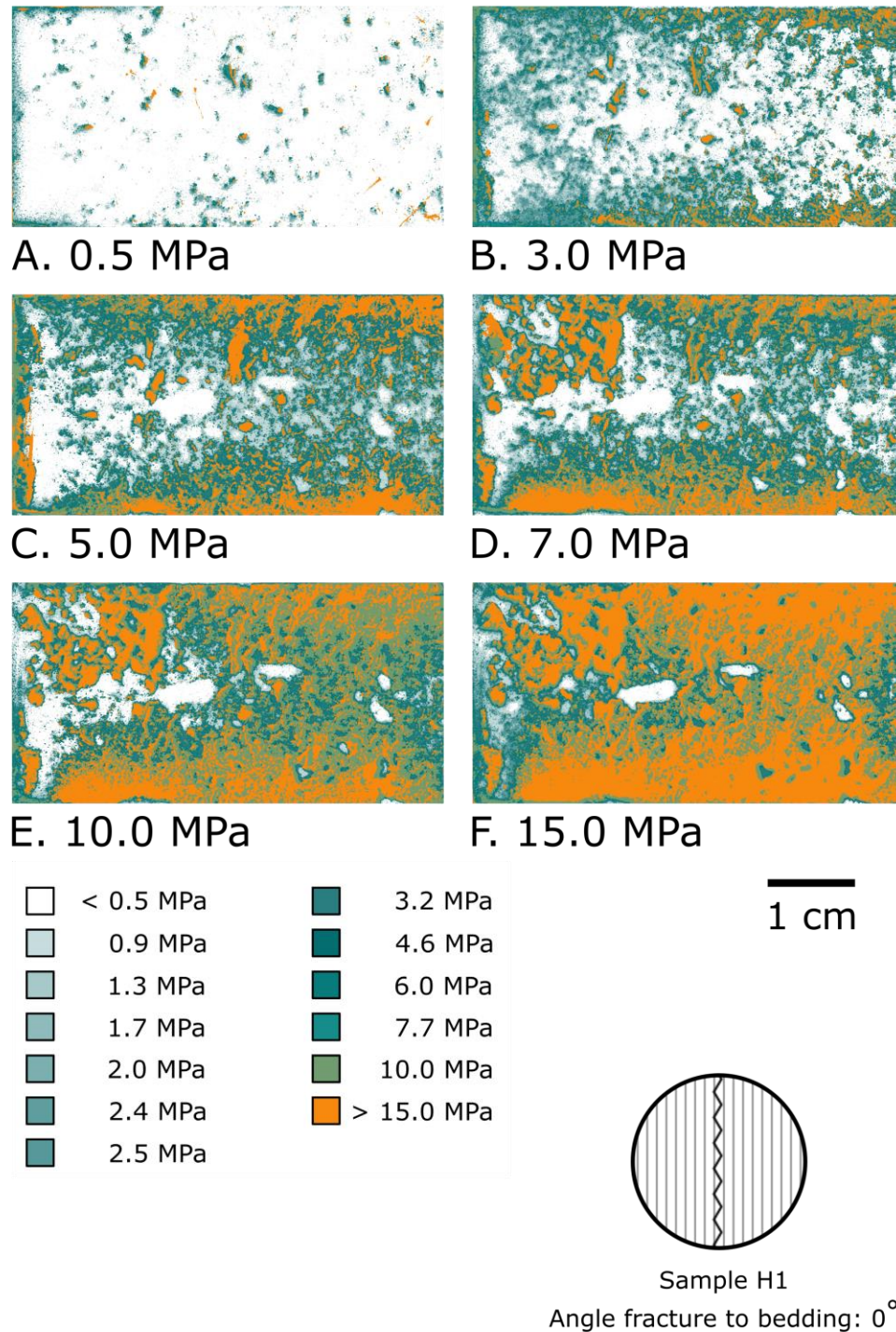


Figure 6 - Stress distribution map of sample H1 from the fractured sample compression experiments.

4.3.1. Results of multiple-stress-steps tests on fractured samples of different bedding angle

4.3.1.1. Fracture compaction

Figure 7 shows three scattered data plots of fracture compaction data. Experiments were performed on three samples, each with a different fracture orientations relative to the bedding. In order to make the scattered data plots a bit more structured, trendlines were implemented in the graph.

All three of these data plots show an increasing trend in fracture compaction with increasing force. However, the slope of these trends differs and shows the lowest value for the sample which fractured along the bedding (H1), the highest value for the sample with a fracture-to-bedding angle of 15° (H20) and shows a value in between these two for the sample with a fracture-to-bedding angle of 30° (H30-1).

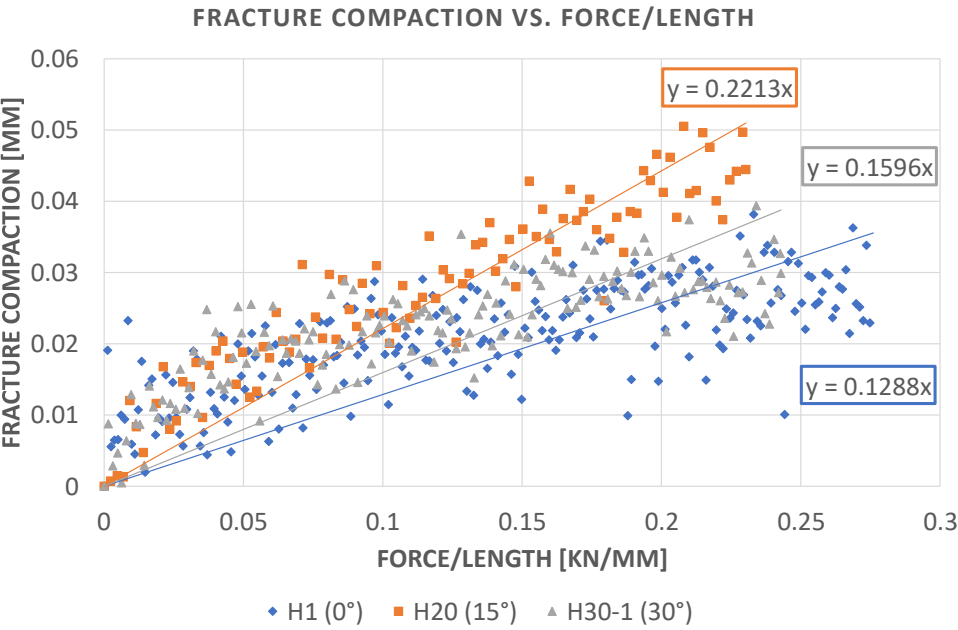


Figure 7 - Scattered data points including trendlines of fracture compaction data extracted from intact and fractured compressibility experiments, performed on samples with different fracture - bedding angles.

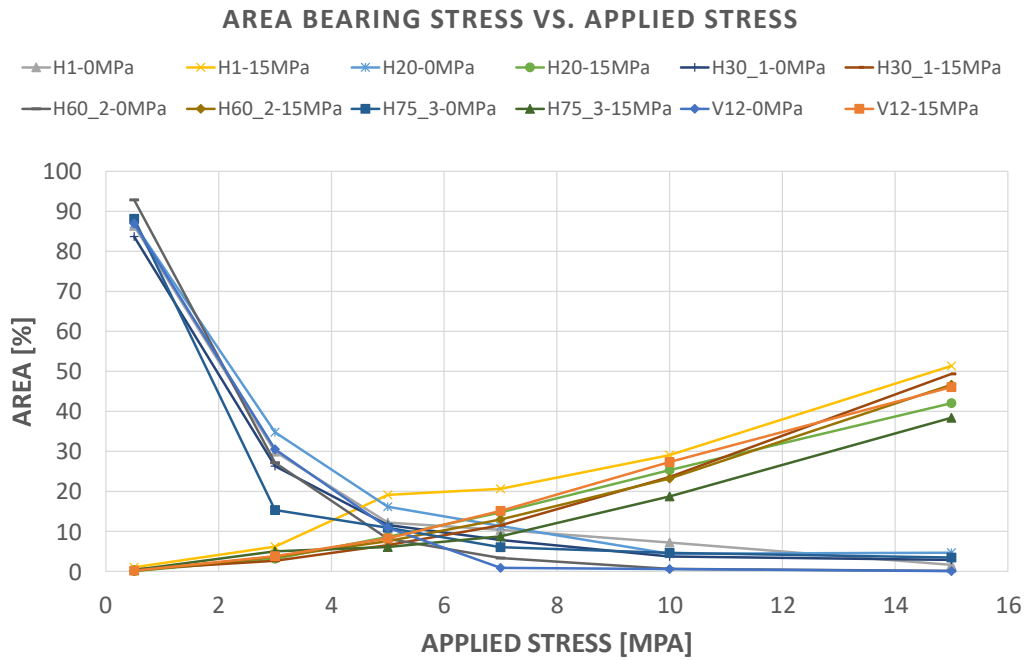


Figure 8 - Free space and 15 MPa-bearing contact areas as a percentage of the total area of the fracture plane plotted against applied stress for all samples with different fracture-to-bedding angles in a range from 0 to 90 degrees.

4.3.1.2. Effect of bedding angle on the free space and 15 MPa-bearing contact areas

All samples in figure 8 show a decreasing trend in free space (blueish colours) with increasing applied stress. At lower applied stresses this decrease rate is more rapid than for the higher applied stresses. This results in a “hockey stick”-like shape with a significant decrease in free space until 7 MPa applied stress and a slight decrease from 7 MPa onward, almost reaching a steady state.

The >15 MPa-bearing contact area increases for all samples with increasing applied stress, from ~0% at 0 MPa to 40-50% at 15 MPa applied stress. At the low applied stresses (< 5 MPa), the area increases by ~2.2%/MPa, but at higher applied stress, the increase in >15 MPa-bearing contact area seems near-linear with ~3.5%/MPa increase.

As there is no clear influence of the fracture-to-bedding orientation on the free space and >15MPa-bearing contact area versus applied stress, data points obtained at the same applied stress but for different bedding orientations are taken together.

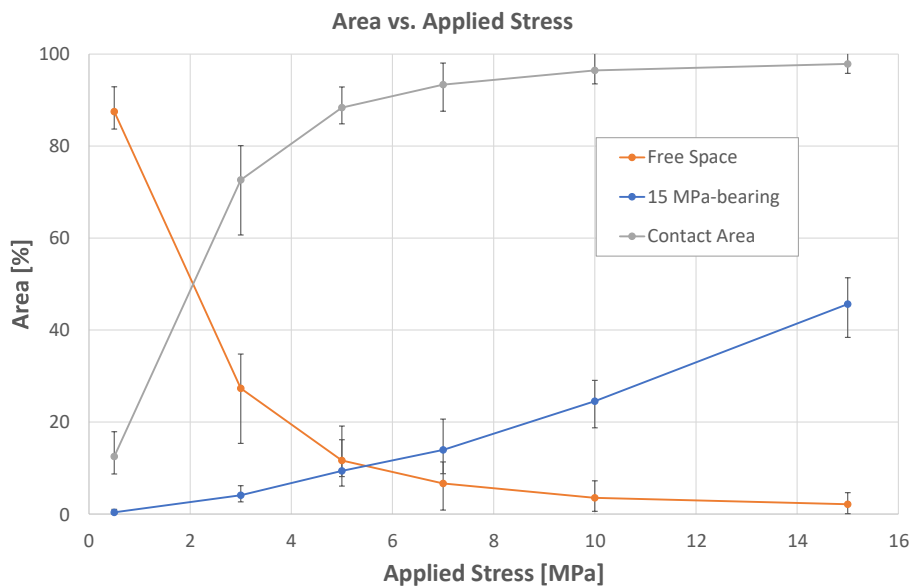


Figure 9 - Plotted averaged datasets of all used samples for both free space area and 15 MPa-bearing contact area. Contact area is provided by subtracting the free space area of the total (100%) area.

All data from experiments with different samples was averaged and plotted as area over applied stress with a rough interpretation of area-data in between datapoints from experiments (Figure 9). Contact area was calculated by subtracting the free space area of the total area (100%). Error bars in vertical direction show the range of datapoints used for the averaging.

As visible in figure 9, the increase in >15MPa-bearing contact area is not taking account for all of the increase in contact area. Therefore, the distribution of stress on the fracture plane was plotted per increasing stress step (Figure 10). At the lower stress steps (0.5, 3.0 MPa), the increase in contact area was mostly accommodated by the increase in lower stress-bearing contact area, whereas the increase in contact area at higher stress steps (5.0, 7.0, 10.0 & 15.0 MPa) was accommodated by the increase in higher stress-bearing contact area.

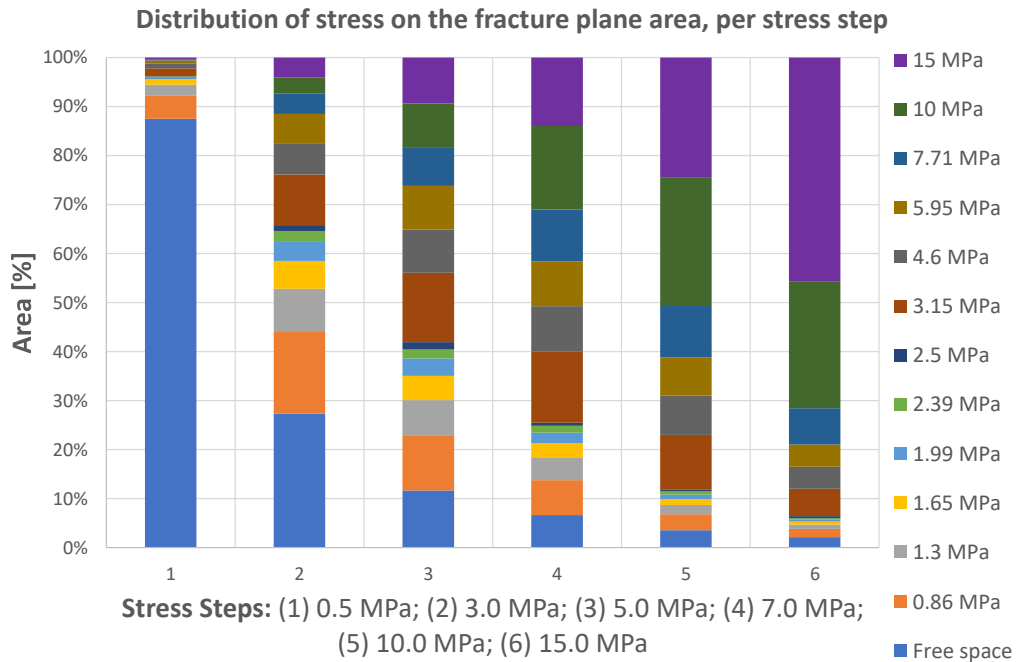


Figure 10 – Column diagram of the distribution of stress on the fracture plane area per stress step. Values used in diagram are average values for each stress step for all samples. These values do not include the errorbars that are visible in figure 6.

4.3.1.3. Effect of bedding angle on the Joint Roughness Coefficient

Fracture planes are scanned at Royal Dutch Shell in Amsterdam, to obtain Joint Roughness Coefficient (JRC) data. In figure 11 the JRC data for each sample is plotted against its accompanying fracture-to-bedding angle. Roughly speaking, the higher the fracture-to-bedding angle, the higher the JRC. The lower this angle, the lower the JRC.

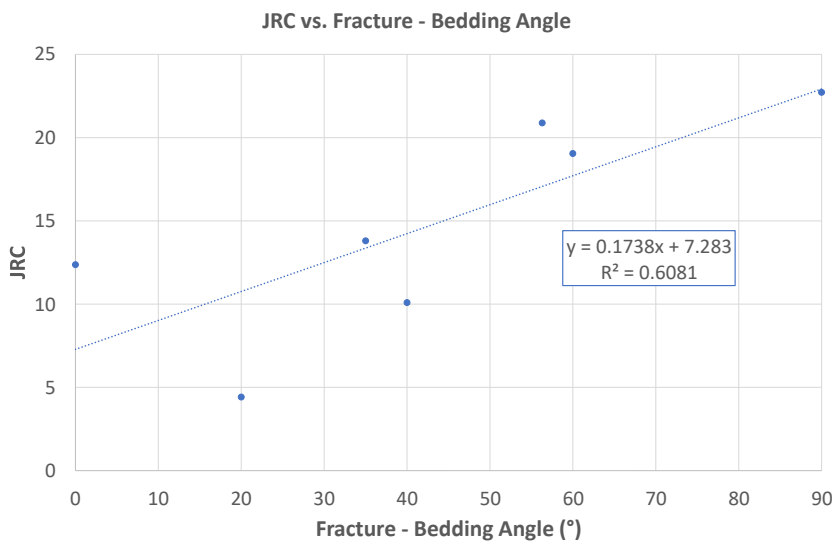


Figure 11 - Joint Roughness Coefficient (JRC) data plotted versus varying fracture-to-bedding angles. Dashed line is a linear fit to the experimental data ($R^2 = 0.6081$).

4.3.2. Results of creep tests: Effect of time & fracture offset

Stress distribution maps of time & offset dependent experiments are shown in Appendix C.

4.3.2.1. Effect of time

All experiments give qualitatively similar results. Visual inspection of the pressure sensitive paper (LLW) used for the longer holding times, show wet patches around the red stains with high colour densities. This visual feature was not captured during the scanning of the PSPs and can therefore not be further included in the results.

With increasing time, a decrease in free space area is observed for all samples. The initial free space area differs due to the influence of fracture offset and applied stress, with ~37.5% less for a higher applied stress (with offset) and ~26% less for a sample with offset relative to a sample without offset under similar stress conditions. After a significant decrease in free space area after a shorter period of time, the decrease starts slowing down, almost reaching a constant value, giving the graph shown in figure 12 a “hockey stick”-like shape (cf. black curves in figure 12, for 5 MPa (solid squares) and 15 MPa (solid triangles) applied stress).

The increase in >15 MPa-bearing contact area slows down with time rapidly resulting in just a slight increase of contact area, even after longer periods of time (> 4 hrs hold time). Figures 13 and 14, and table 4 show this almost constant percentage of contact area with increasing time for the >15 MPa-bearing contact area.

Table 4 - Percentages of free space area and >15 MPa-bearing contact area at each given time.

	V3 @ 15 MPa		V2 @ 5 MPa	
Hours under stress	Free space [%]	>15 MPa-bearing area [%]	Free space [%]	>15 MPa-bearing area [%]
0.25	26.46	33.23	63.92	10.57
1.25	16.68	35.51	58.68	11.29
5.25	10.99	36.51	53.59	12.23
21.25	5.32	36.17	43.84	12.73
45.25	4.17	38.10	37.49	12.43
113.25			34.47	12.83

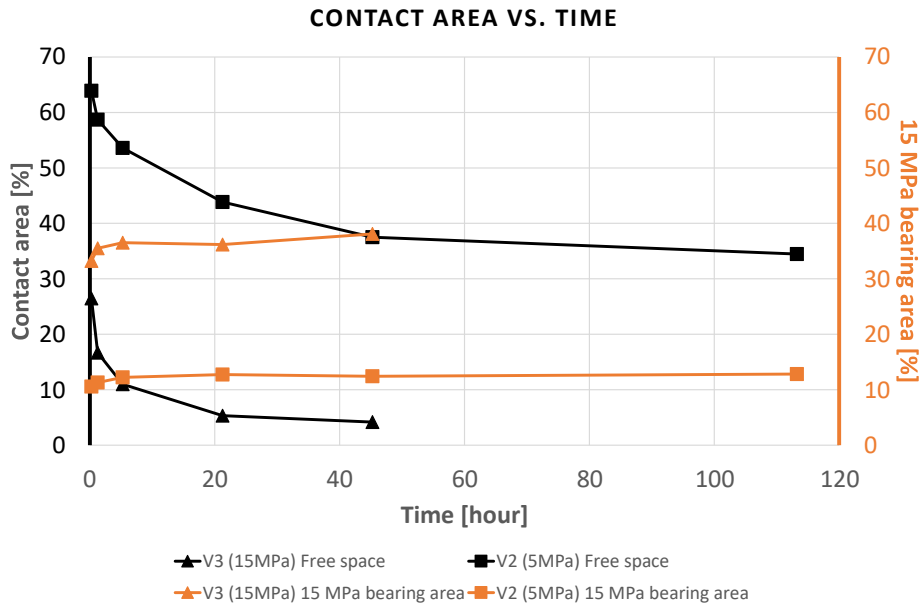


Figure 12 - Area of free space and >15 MPa-bearing contact area as a percentage of the whole fracture plane over time. Samples used are from the V-series, meaning the fracture-to-bedding angle is 90°.

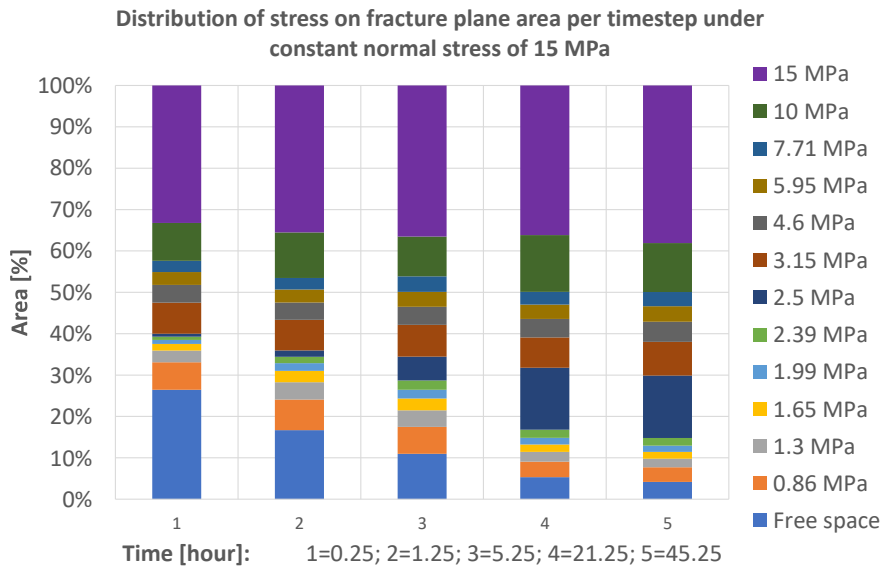


Figure 13 - Column chart of the percentage of the contact area per defined contact stress. Experiments performed on sample V3, constant applied stress of 15 MPa.

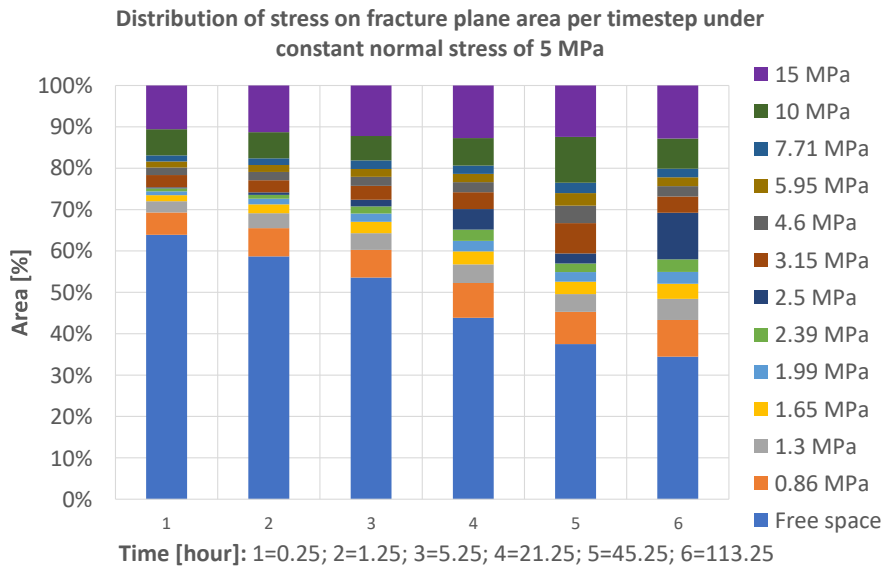


Figure 14 - Column chart of the percentage of the contact area per defined contact stress. Experiments performed on sample V2, constant applied stress of 5 MPa.

4.3.2.2. Effect of fracture offset

Looking at sample V3 with an initial offset of 1.5 mm compared to the sample V14-01 which had no initial displacement, but both a constant applied stress of 15 MPa, the similarity of increasing contact area with increasing time is visible. This increase seems less for V14-01 as the initial contact area is higher due to the “perfect fit” of the two halves of the sample. The contact area is shown in the Appendix C, as every coloured pixel in the stress distribution maps contributes to the contact area along the fracture plane.

Both of the samples can be considered similar as the fracture-to-bedding angle is constant, the applied stress is constant, resulting in one variable, which is the initial offset. This variable results in some differences in the outcome of these two experiments. As is shown in figure 16 the initial contact area is less for the sample (V3) for which the offset was included, than for the sample without initial offset (V14-01).

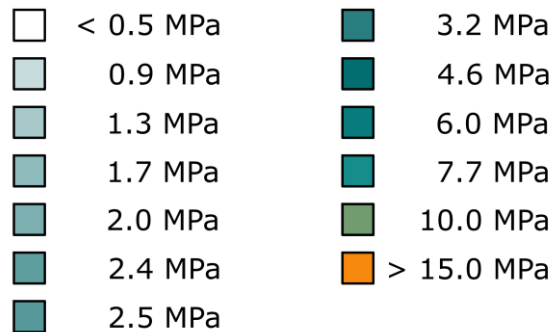


Figure 15 - Legend for upcoming stress distribution maps.

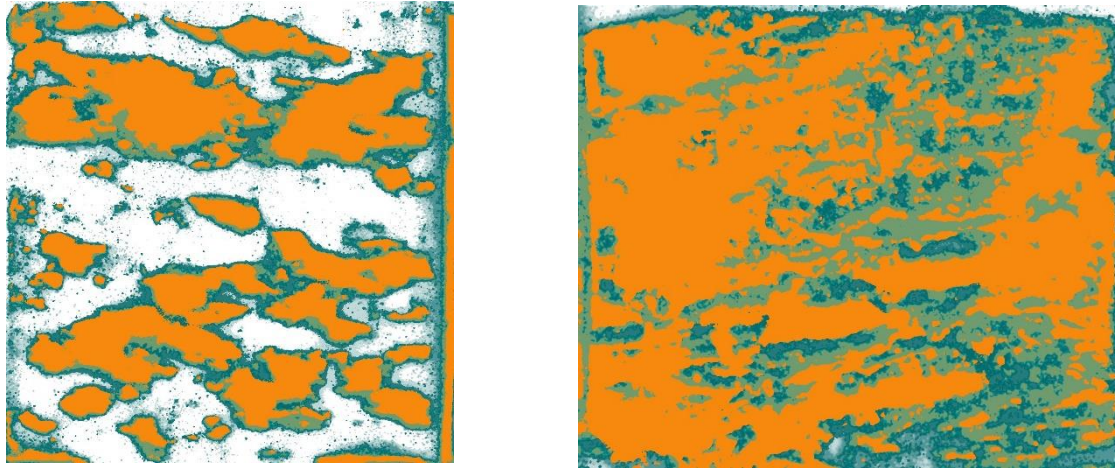


Figure 16 - Stress distribution on the fracture plane of Sample V3 versus Sample V14-01 after subjecting to constant normal stress of 15MPa for 15 minutes. Left figure: sample V3 tested with a including initial offset of 1.5 mm; the right figure: sample V14-01 without initial offset. White areas are areas bearing a stress less than 0.5MPa, hence considered as free space. Legend for these stress distribution maps is shown in figure 15.

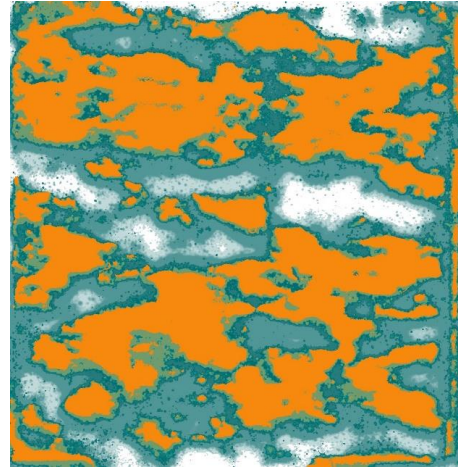
Sample V14-01 shows an almost full contact after ~15 minutes and a ~100% >15 MPa-bearing contact area after 4 hours (Figure 17). Whereas for sample V3, there is no full contact reached after the full extent of the experiment as shown in figure 18. As shown in figure 13, there is no large increase in >15 MPa-bearing contact area and most of the increase in contact area is accounted for by the increase of 2.5 MPa-bearing contact area along the sides of the >15 MPa-bearing contact area, which is visible due to the increase of blue coloured pixels (2.5 MPa-bearing) along the sides of the orange areas (>15 MPa-bearing) in Appendix C.

Figure 17 - Stress distribution map of sample V14-01 after 4 hours under constant stress of 15 MPa. All coloured pixels contribute to the total contact area along the fracture plane, whereas the orange coloured pixels account for the >15 MPa-bearing contact area. Legend for stress distribution map is shown in figure 15.



In order to distinguish the influence of applied stress on the contact area on a fracture plane including an initial displacement, the experiment executed on sample V2, which was performed with an applied stress of 5 MPa, can be taken into account. The only variable between the experiments performed on sample V3 and sample V2 is the quantity of applied stress.

Figure 18 - Stress distribution map of sample V3 after the full extent (24 hours) of the experiment under constant stress of 15 MPa. All coloured pixels contribute to the total contact area, the orange coloured pixels account for the >15 MPa-bearing contact area. Legend for stress distribution map is shown in figure 15.



Both samples show an increase in contact area over time which is shown in figure 12. Figure 12 shows a decrease of free space area with increasing time for both sample V2 as sample V3. As shown in figure 12, which was validated by figures 13 and 14, there is no large increase in >15 MPa-bearing contact area with increasing time. The small increase at the beginning of the experiments reaches an almost constant value after approximately 5 hours for both experiments. Shown by figures 13 and 14 is that the overall increase of contact area is accounted for by the increase of 2.5 MPa-bearing contact area. With time the percentage of ~2.5 MPa-bearing area increases significantly in comparison to the areas that bear lower and higher stresses. For sample V2 there is a small decrease for the 2.5 MPa-bearing area after ~45 hours, the decrease at this point is mostly compensated by an increase in 3.15 and 10 MPa-bearing contact areas as is shown in figure 14.

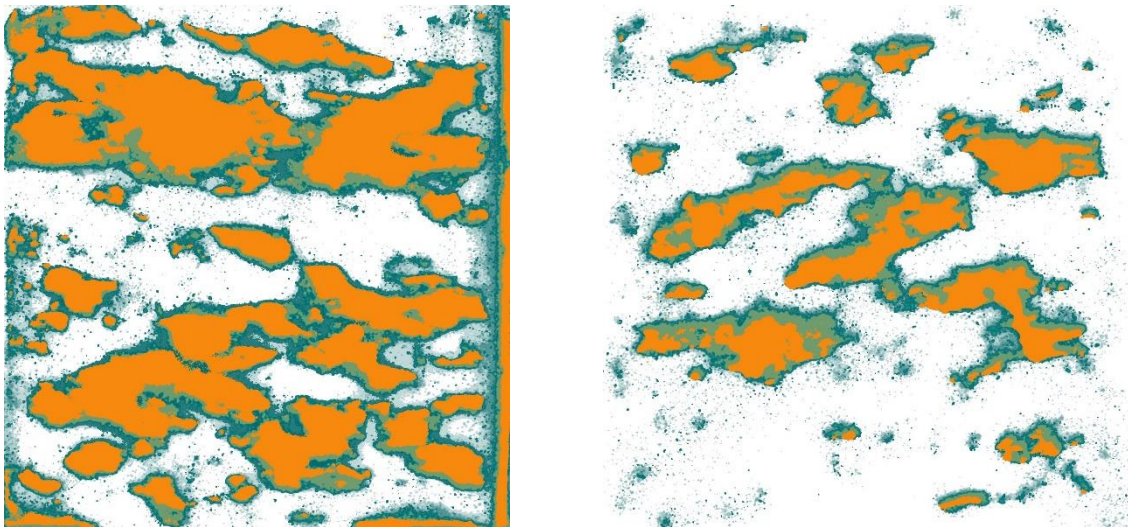


Figure 19 - Left figure shows the stress distribution map of sample V3 after 15 minutes under stress. The right figure shows the stress distribution map for sample V2 after 15 minutes under stress. All coloured pixels contribute to the total contact area. Both figures are snapshots from the more elaborated overview of the results of these experiments which are shown in Appendix C. Legend is shown in both Appendix C and figure 15.

The influence of difference in quantity of applied stress is mostly visible in the initial contact area for both samples. Sample V3 which underwent a constant stress of 15 MPa for the full extent of the experiment, shows a higher initial contact area in comparison to the experiment in which sample V2 underwent a constant stress of 5 MPa with increasing time. Values for free space area are for both samples are shown in table 4 and are made visible in figure 12.

Sample V3 shows a larger amount of orange coloured pixels (>15 MPa-bearing area) in comparison to sample V2, which is visible in figure 19 and in more detail in figure 12 and table 4. The larger amount of >15 MPa-bearing contact area for sample V3 which is accompanied with a lower initial free space area results in a low free space area after 24 hours of about 5%. On the other hand, sample V2 reaches a value of ~37.5% of free space area after 24 hours and remains at ~35% after an even longer time span of 68 hours. The decrease in free space area reaches an almost steady state after ~22 hours for V3 as the same happens for sample V2 after ~45 hours under constant stress.

5. Discussion

5.1. Intact compressibility experiments

These intact compressibility experiments were performed in order to get the matrix compressibility which can be used for calculating the fracture compaction at a given applied stress. Five samples were used, all with a different bedding orientation. Plotting compaction against force per unit length for all five samples shows a distribution of matrix compressibility for different bedding orientations, as shown in figure 5. The lower the angle (0°), the more compaction occurs with increasing applied force, the higher the angle (90°), the less compaction with increasing applied force.

This overall distribution has to do with the difference in compressibility between the bedding, which is the alternation of mineralogically different layers, which often results in an alternation of harder and softer material. Sample which was compressed with a bedding orientation along the horizontal axis (0°), needs less applied force to reach a certain amount of compaction as the compaction is mostly accounted for by the softer material in between the bedding. The sample with a bedding orientation along the vertical axis (90°), shows that more applied force is needed in order to reach the same amount of compaction. This is due to harder material that makes up the bedding. More force is needed in order to compress this material.

The samples with angles between 0° and 90° show a distribution along a decreasing trend in compressibility. The higher the angle (up to 90°) the lower the compressibility. In order to interpolate between the angles that were tested during the experiments the compressibility data is plotted against the bedding angle (Figure 20). This data can be interpreted as a linear fit, but can also be interpreted as a S-shaped fit. This S-shaped fit, also shown in figure 20, more logically explains the distribution of data shown in figure 5B. Closer to 0° bedding angle more low bedding angle compressibility data is found (15°) and closer to 90° bedding angle also 75° bedding angle compressibility data is found. The 45° bedding angle compressibility data is plotted somewhere in the middle. This higher data density on the edges of the experimental range indicates a S-shaped fit for the data. This S-shaped fit will probably get a more solid underpinning when more intact compressibility experiments are carried out on samples with different bedding orientations.

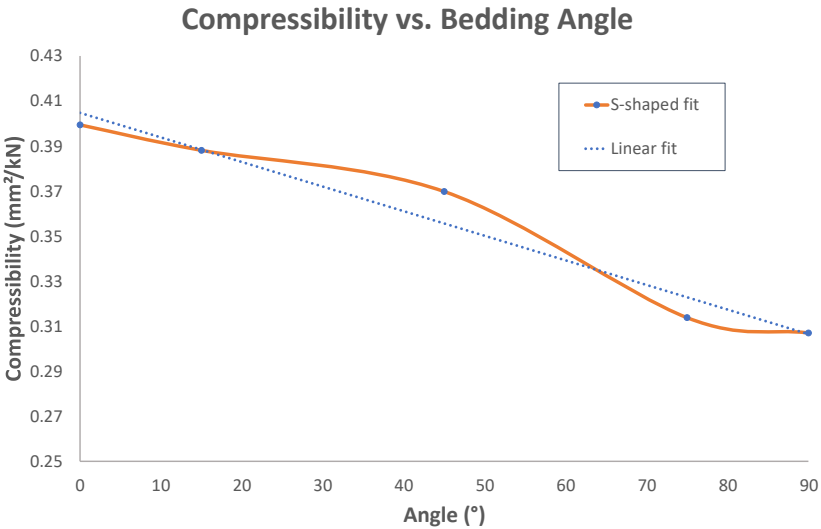


Figure 20 - Plotted experimental intact compressibility data. Dotted line shows linear fit and solid orange line shows S-shaped fit through all data points.

5.2. Comparison of tensile strength and fracture toughness with previous research

All samples were fractured using the Brazilian splitting method suggested in this study (Figure 2). Samples from the V-series where fracture-to-bedding angle was always 90° and samples from the H-series where fracture-to-bedding angle varies in order to be able to look into the influence of bedding orientation on the results of the following experiments. As described by *Chandler et al. (2016)*, material which includes bedding consists of material with different properties. As for the samples used in this study, the material of which the bedding is made can be characterized as harder material and the interbedding material can be characterized as softer material. The softer material is easier to fracture and as fractures follow the easiest way of propagating, this softer material will fracture. Therefore it is hard to fracture samples on a certain angle relative to the bedding orientation. Fractures will and can deflect up to angles of 90° when following the weakest route through the material [*Chandler et al., 2016*].

Large amounts of research on the mechanical behaviour of the Opalinus shale has been done by researchers at the Mont Terri URL. In the study of *Bossart & Thury (2008)* values for the tensile strength of the material have been given. These values can be used for comparison. *Bossart & Thury (2008)* show values of 1.0 MPa normal to bedding and 2.0 MPa parallel to bedding. Experimental data from this study shows values of ~4.0 MPa (Table 3) for parallel to bedding experiments. These values are slightly higher than measured by *Bossart & Thury (2008)*, but water content might play a role in this difference. As stated by *Bossart & Thury (2008)*, the in situ water content of the Opalinus shale at Mont Terri URL is on average ~7% of dry weight of the material. This water content is lower than the samples used for the experiments in this study. Lower water content lowers the strength of the material, as more microcracks start to form due to dehydration of the sample. These microcracks form weak spots in the sample and this might account for the difference in tensile strength between the results from *Bossart & Thury (2008)* and the experimental results from this study.

Using the experimental output for the tensile strength of the material as input for the calculation of the fracture toughness by the trend of *Chandler et al. (2016)* gives values that are in line with the experimental results discussed in the Technical Report by *Bock (2001)*. Values given in this Technical Report are $0.53 \pm 0.09 \text{ MN/m}^{1.5}$ for samples that are similar to the ones used in experiments for this study and $0.12 \pm 0.03 \text{ MN/m}^{1.5}$ for samples where direction of fracture opening is perpendicular to bedding orientation.

Values for fracture toughness calculated from the tensile strength and the trend predicted by *Chandler et al. (2016)* are similar to the fracture toughness given by *Bock (2001)* which calculated the fracture toughness by using the *ISRM (1988)* method.

5.3. Compression of fractured shales

5.3.1. Effect of bedding orientation

5.3.1.1. Fracture compaction

Fracture compaction data was extracted from the fractured compressibility tests by subtracting the matrix compressibility measured during the intact compressibility tests. Due to the difficulty of fracturing samples along the desired fracture-to-bedding angle, sample H20 underwent intact compression at an angle of 20°, but underwent fractured compaction at an angle of 15°. The fracture compaction data, which was subtracted from these two data sets combined, will be slightly off. Figure 21 shows the trendlines that were also shown in figure 7, but without all the data points.

It would be expected that the fracture compressibility would depend on the fracture-to-bedding angle as this angle plays a role in the roughness of the surface. Following the results from this study, shown in figure 21, there is no clear trend visible for the influence of bedding orientation in the compaction of fractures with applied force.

The lack of trend in this data will most likely be caused by the lack of samples along the whole scale of bedding orientations. Only data at low fracture-to-bedding angles is shown in figure 21. Larger angles might give the larger overview and will probably result in some relationship between fracture-to-bedding angle and fracture compaction. This can be the infill for further research on the compaction of fractured Opalinus Clay shales.

During these fracture compaction tests, only samples without initial displacement are tested. All samples tested had a perfect fit of the two halves of the sample at the start of the compressibility test. Therefore fracture compaction data only shows results for fractures that did not have an artificial 'slip-event'.

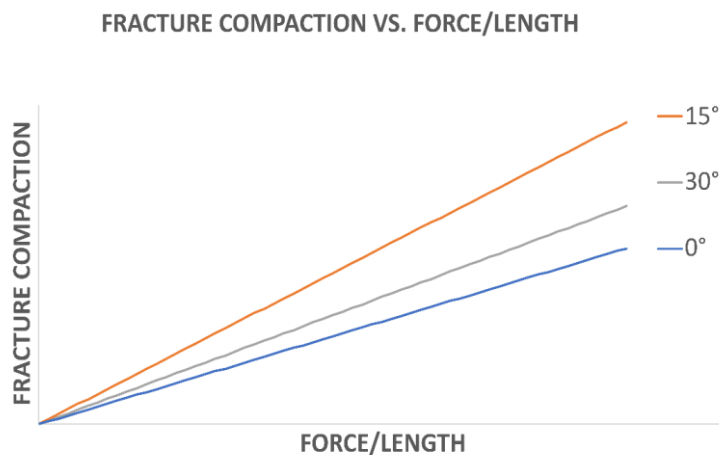


Figure 21 - Trendlines that resulted from the plotting of all data points for fracture compaction. There seems to be no relationship between the fracture-to-bedding orientation and the fracture compaction within the range of this experiment..

5.3.1.2. Effect of bedding angle on the free space and 15 MPa bearing contact areas

Results show a clear trend in both decrease of free space area and increase in >15 MPa-bearing contact area with increasing applied stress. There is no influence of the orientation of the bedding. Due to this lack of influence of the bedding orientation, it is possible to set up an empirical model for both free space area and >15 MPa-bearing contact area with increasing applied stress. This prediction is shown in figure 22 and values for these predictions are given in table 5, where they are compared to the experimental data range.

Table 5 - Range for experimental data for both free space area and >15 MPa-bearing contact area and the error on the predicted values.

Applied stress [MPa]	Free space area [%]		>15 MPa-bearing contact area [%]	
	Experimental data range	Predicted value	Experimental data range	Predicted value
0.5	92.89 - 83.70	83.95	1.02 - 0.08	1.33
3.0	34.79 - 15.36	34.99	6.17 - 2.65	7.99
5.0	16.16 - 8.14	17.38	19.13 - 6.08	13.32
7.0	11.33 - 0.86	8.63	20.64 - 8.77	18.64
10.0	7.22 - 0.59	3.02	29.06 - 18.75	26.63
15.0	4.65 - 0.08	0.52	51.37 - 38.40	39.95

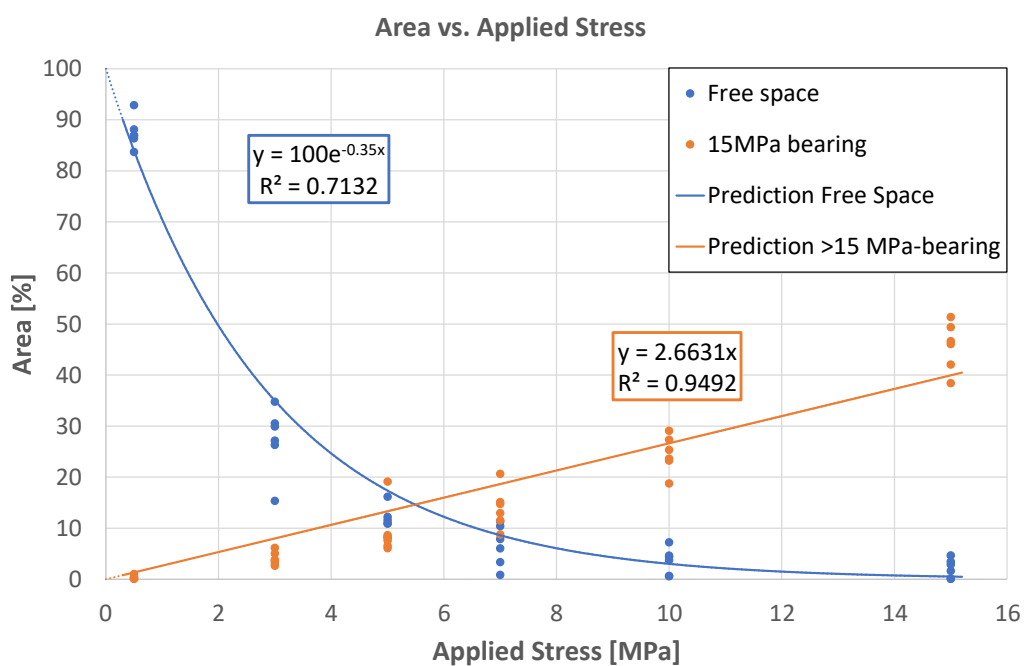


Figure 22 - Plotted experimental data for Free space area and >15 MPa-bearing contact area with increasing Applied Stress. Exponential trend is chosen as best fit for Free space area prediction and a linear fit is chosen for the >15 MPa-bearing contact area prediction.

Plotted are the most realistic fits for the prediction of both free space area and >15 MPa-bearing contact area with increasing applied normal stress on the fracture plane.

$$\text{Free space area } (\sigma) = 100e^{-0.35*\sigma}$$

Where σ is the applied normal stress on the fracture plane [MPa] and the free space area is a percentage [%] of the total area of the fracture plane.

$$> 15 \text{ MPa} - \text{bearing contact area } (\sigma) = 2.6631 * \sigma$$

Where σ is the applied normal stress on the fracture plane [MPa] and the >15 MPa-bearing contact area is a percentage [%] of the total area of the fracture plane.

Predictions can only be made within the range of experimental data as the trendline is not tested outside of this range and therefore not proven valid.

An exponential fit was chosen as the best fit for the free space area prediction. This fit was chosen in order to fit the steep decline in area at start and the ability to set an intersect at 100%. Trendline for free space area shows a prediction value that is slightly higher than the experimental data at applied normal stresses of 3.0 MPa, but the predicted value for applied normal stresses of 0.5, 5.0, 7.0, 10.0, 15.0 MPa are within the experimental data range.

For the prediction of >15 MPa-bearing contact area a linear fit was chosen due to the almost linear increase of the experimental data with increasing applied normal stress. At applied normal stresses of 0.5 and 3.0 MPa the predicted values is slightly higher than the experimental data range, but for the higher applied normal stresses within the range of the experiment, the predicted values lay within the experimental data range.

All this data was gathered from the stress distribution maps shown in Appendix B. These illustrations give an estimate of the stress distribution along the fracture plane for different applied normal stresses on the fracture planes of samples with different fracture-to-bedding orientations. They are estimations as there are a few errors that may have been introduced along the process of the digital image processing and analysis.

First, the colour of the ink in the PSP is an indication for the stress intensity, which can be coupled to a certain stress level born at each location. However, this ink slightly loses its colour intensity with increasing time. As not all PSPs are scanned within the same timespan after the PSP experiment, colour might have changed slightly, resulting in slightly different values for the stress born at each location.

Second, three different PSPs are used for each applied stress. These three PSPs are scanned, cropped and aligned manually. Human errors might play a role in this and a shift in the alignment can result in a different stress at a certain location. This error is not significant, but might play a role in the amount of free space area calculated by using the final stress distribution maps (Appendix B).

Finally, the stiffness of the PSPs will influence the print on the PSP itself. At some parts it might not bend so easily and therefore increase the stress that seems to be applied to a certain part of the sample but this extra stress is only applied due to the PSP itself and should not be part of the stress distribution values.

5.3.1.3. Effect of bedding angle on the Joint Roughness Coefficient

Figure 11 roughly shows a relationship between Joint Roughness Coefficient (JRC) data and fracture-to-bedding orientation. The lower the fracture-to-bedding angle, the lower the roughness of the fracture plane. The higher the fracture-to-bedding angle, the higher the roughness of the fracture plane. This increase in roughness with increasing fracture-to-bedding angle only accounts for the angles between 0° and 90°. Angles higher than 90° will give similar values than the ones lower than 90° as the sample will behave in a symmetrical way.

Shown in figure 11 is the error between the experimental data from the sample that fractured along the bedding (0°) and the predicted JRC value for this sample. As the sample fractured along the bedding, the roughness of the fracture surface will highly depend on the initial roughness of the bedding itself. Initial roughness of the bedding plane can vary due to its depositional history, but further research is needed in order to get a trend for this initial roughness. For the higher fracture-to-bedding angles the trendline has a better fit to the experimental data. *Yong et al. 2018* used data from previous research in order to assemble ten standard surface profiles with their corresponding JRC-values in order to give some idea on how the surface looks like at a certain JRC value (Figure 23).

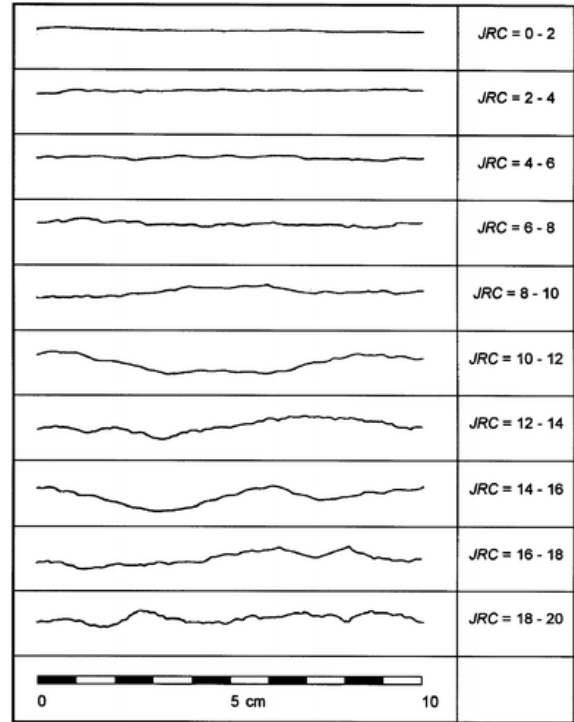


Figure 23 - Ten standard profiles with their JRC-values (*Yong et al., 2018*).

5.3.2. Effect of time & offset

5.3.2.1. Effect of time

The effect of time shows that free space area keeps decreasing with time even though this decrease in free space area slows down very rapidly after a short amount of time. If a fracture in this type of clay-rich material would experience a slip event, the contact area will decrease for a short time due to the displacement of the asperities on the fracture surface. They will not align perfectly which will decrease the stress-bearing contact area. Over time the free space area will decrease again, possibly until a contact area of ~100% is achieved.

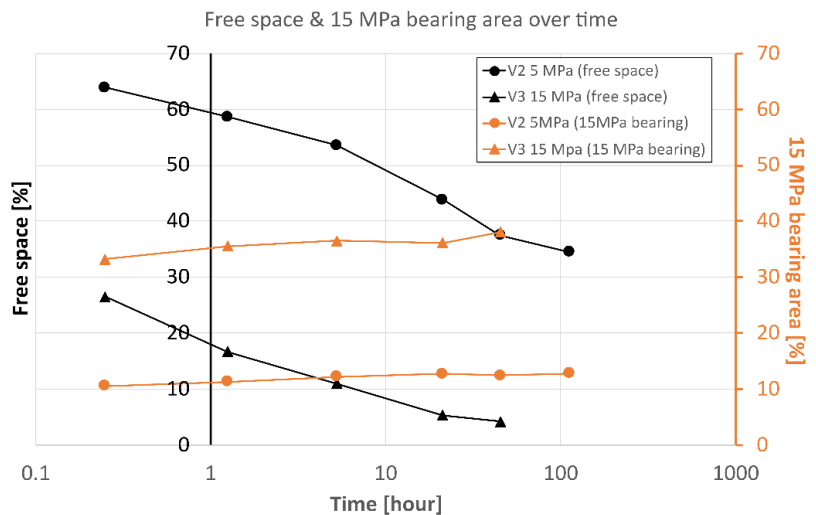


Figure 24 - Free space area and >15 MPa-bearing contact area plotted over logarithmic time.

The smaller the decrease in contact area due to the slip event, the faster this area will return to its original level, the larger this decrease in contact area, the longer this process will take.

The evolution of both free space area and >15 MPa-bearing contact area with time appears to have a logarithmic dependence (Figure 24). The roughly straight line can be extrapolated for longer timespans and therefore give a rough estimation on the evolution of free space and load bearing areas on the fracture plane, which gives an indication for the time it will take for the fracture to close/heal itself. Following formulas are obtained from this logarithmic fit:

$$\text{Free Space Area}_{5\text{ MPa}} = -5.086 * \ln(\text{time}) + 58.917$$

$$\text{Free Space Area}_{15\text{ MPa}} = -4.298 * \ln(\text{time}) + 19.051$$

Sample V3 (15 MPa) reaches a free space area of less than 5% after the timespan of this experiment, approximately 45 hours. Sample V2 (5 MPa) reaches a free space area of ~35% of the total fracture plane area after the full extent of the experiment (~113 hours). In order for sample V2 (5 MPa) to reach this 5% free space area value of sample V3 (15 MPa) it will take roughly 4.6 years. Further research is needed in order to distinguish the maximum free space area on a fracture plane for the fracture to be nonpermeable as the free space area does not have to be 0% for a fracture to be nonpermeable.

5.3.2.2. Effect of offset

Formulas for free space area predictions shown above are for samples where initial displacement, or mismatch, was introduced to the samples. The experiments including the initial offset can be seen as experiments that start after sliding along the fracture plane, but does not include the damages to the asperities on the surface and the smearing of the material which will impact the contact area and the permeability. Due to the misalignment of the asperities on the fracture surface, the contact area decreases, opening up the fracture, increasing permeability and the leakage potential. The outcome of these experiments in combination with the variable of time show that fractures will heal themselves over time. Therefore it can be inferred that fractures that are present in an Opalinus shale, or clay-rich, caprock will be likely to close with increasing time. This healing process will happen at a rate which depends on the in situ normal stress acting on the fracture plane. Over time, there is hardly any change visible in the V3/V2 (Figure 25).

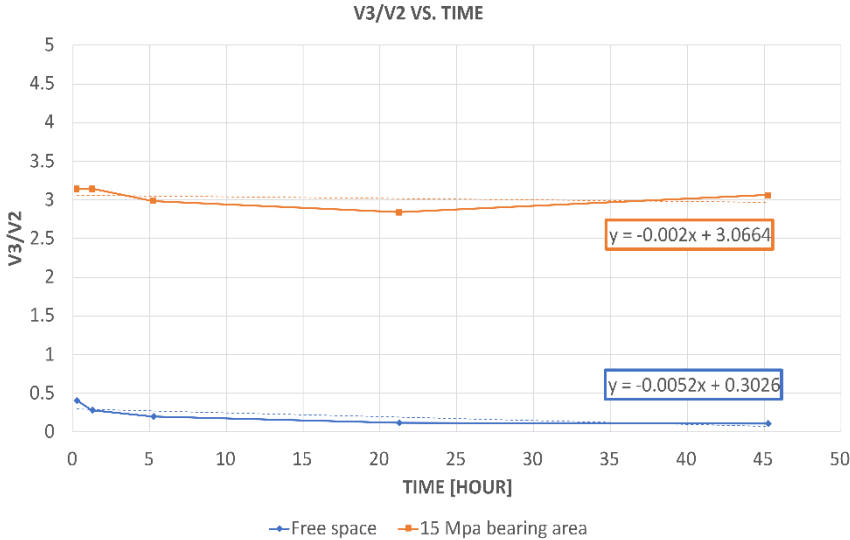


Figure 25 - Ratio of the free space area, and >15 MPa-bearing contact area, for samples V3 (15 MPa normal stress) and V2 (5 MPa normal stress), shown as (contact area V3)/(contact area V2) versus time.

The slope of the trendlines in figure 25 are nearly zero, i.e. there is no change in this ratio with time. This results in two ratios. Ratio V3/V2 for free space area gives the following results:

$$\frac{V3 (15 MPa)}{V2 (5 MPa)} = 0.3026$$

$$V3(15 MPa) = 0.3026 * V2 (5 MPa)$$

The free space area for sample V3 (15 MPa) is ~0.3 times the free space area of sample V2 (5 MPa) which is close to the ratio between the applied stresses for V3 (15 MPa) and V2 (5 MPa), which makes the free space area inversely related to applied stress. This inverse relationship stops at a certain point where there is just no more free space area due to the applied normal stress on the fracture plane, therefore this inverse relationship holds in the range of this experiment and can just be extrapolated to slightly higher stresses.

The ratio V3/V2 for >15 MPa-bearing contact area gives the following results:

$$\frac{V3 (15 MPa)}{V2 (5 MPa)} = 3.0664$$

$$V3 (15 MPa) = 3.0664 * V2 (5 MPa)$$

The ratio shows that the >15 MPa-bearing contact area is ~3 times larger for V3 (15 MPa) than for V2 (5 MPa), which shows the same ratio as V3/V2 for applied normal stresses. The relationship for >15 MPa-bearing contact area shows a linear relationship to the applied stress, within the range of experimental data. It cannot be stated that this linear relationship holds up outside of this range of applied normal stresses.

5.3.2.3 Possible mechanisms causing time-dependent deformation of the fracture surface

Visible in figure 13 and 14 is the fact that the 2.5 MPa-bearing contact area accounts for most of the increase in overall contact area for both sample V2 (5 MPa) as sample V3 (15 MPa) while there is hardly any visible increase in >15 MPa-bearing contact area. Visual analysis of the fracture surfaces shows dried out patches on the samples fracture surface which correspond with the highest stress bearing parts of the contact area. (Figure 26)

These dried out patches might have made the sample locally more brittle, resulting in more micro fractures and therefore the sample could not bear more than a stress of 2.5 MPa as the yield stress dropped drastically due to this stress-induced drying out of the sample.

There is one main question that remains. Why did the sample dry out? PSP seemed to have taken up a bit of fluid from these dried out high stress bearing contact points, which was slightly visible after the experiments but unfortunately not captured during the scanning of the PSPs. *Zhang (2019)* performed experiments on the stress-strain-sorption behaviour of smectites in which he used montmorillonite as his smectite sample. *Zhang (2019)* stated that the time-dependent release of CO₂ and/or H₂O from the sample occurred due to reversible stress-induced desorption. This rate of H₂O and/or CO₂ desorption is known to be rapid (for montmorillonite) and *Zhang (2019)* suggests that this time-dependent effect is mainly controlled by the samples permeability for H₂O and/or CO₂.

This process of time-dependent desorption of liquid, in this case H₂O, corresponds to the visual features of the wet parts of the PSPs used during the time-dependent experiments as described in the results section (4.3.2). Further research objectives can include quantifying this time-dependent stress-induced desorption of liquid from the asperities on the fracture surface and its influence on the mechanical behaviour of fractures.



Figure 26 - Fracture surface of sample V2 after time dependent experiments. Light grey spots correspond with areas of higher stress bearing contact. Light grey patches seem to be dried out as the surrounding matrix colour is dark grey. Light grey patches have lost their roughness which can be linked to the fact that stress was applied to the fracture surface.

6. Conclusions

During the experiments, the main aim has been to obtain empirical relationships describing the fracture roughness evolution, and therefore contact area and stress distribution, as a function of time and stress. These empirical relationships are of importance for usage in numerical first-order assessment models of the leakage potential of fractures in clayey caprock under different storage conditions. The main findings of the present research are as follows:

1. The effect of bedding orientation

- a. The intact compressibility tests show a relationship of low compressibility for samples with bedding orientation of 90° and high compressibility values for samples with bedding orientations closer to 0°.
- b. Data from the fracture compaction experiments are not sufficient to show any form of trend. More research is needed especially including samples for a larger scale of bedding orientations.
- c. There is no clear effect of bedding orientation on the evolution of free space area with varying applied stress. All samples with varying bedding orientations behave the same under different applied stresses. Overall trend visible in data gives prediction of:

$$\text{Free space area } (\sigma) = 100e^{-0.35*\sigma}$$

- d. There is also no clear effect of bedding orientation on the evolution of >15 MPa-bearing contact area with varying applied stresses. Overall trend visible in data gives prediction of:

$$> 15 \text{ MPa} - \text{bearing contact area } (\sigma) = 2.6631 * \sigma$$

- e. The effect of bedding orientation on the Joint Roughness Coefficient (JRC) values of the fracture surfaces shows an increasing trend with increasing angle. The higher the fracture-to-bedding angle, the higher the JRC value. Roughness of fracture surface along the bedding highly depends on the initial roughness of the bedding and is therefore hard to predict. Predictive trend visible in experimental data from this study can be captured in the following formula:

$$JRC = 0.1738 * \theta + 7.283$$

Where θ is the fracture-to-bedding angle ($0^\circ < \theta < 90^\circ$).

2. The effect of time

The evolution of contact area and stress distribution shows similar trends for different applied stresses. The predictive trend which was obtained by putting time on a logarithmic scale, gives the following formulas for free space area over time:

$$\text{Free Space Area}_{5 \text{ MPa}} = -5.086 * \ln(\text{time}) + 58.917$$

$$\text{Free Space Area}_{15 \text{ MPa}} = -4.298 * \ln(\text{time}) + 19.051$$

3. The effect of offset

The decrease in free space area with increasing time implies the self-healing of the fracture with time. Both the evolution of contact area and stress distribution show similar trends. Increase in contact area seems to be accounted for by the increase of ~2.5 MPa-bearing contact area instead of >15 MPa-bearing contact area. This can be explained by the stress induced drying out of the contact areas asperities. Due to this drying out of the contact areas, the material starts to act in a more brittle way, creating microfractures and decreasing the yield stress of the material. Due to this drop in yield stress the material is not able to hold the higher stress >15 MPa. More research is needed to better understand the influence of time-dependent stress-induced desorption of the fracture surface on the mechanical behaviour of a fracture.

Acknowledgement

Hereby I would like to express my dearest gratitude to: M. Zhang for guiding me through the experiments, providing me with his knowledge about the topic, our weekly meetings and for reviewing my thesis; S.J.T. Hangx for reviewing my thesis, our weekly meetings and guiding me through the end stage of this project; and B.M.G. Vermeulen for scanning the fracture surfaces at Royal Dutch Shell and providing me with his data.

References

- Bock, H. (2001).** RA Experiment, Rock Mechanics Analyses and Synthesis: Data Report on Rock Mechanics, *Technical Report 2000-02 July 2001, Q+S consult, Germany*.
- Bossart, P., Bernier, F., Birkholzer, J., Bruggeman, C., Connolly, P., Dewonck, S., ... & Wieczorek, K. (2017).** Mont Terri rock laboratory, 20 years of research: introduction, site characteristics and overview of experiments. *Swiss Journal of Geosciences*, *110(1)*, 3-22.
- Bossart, P., & Thury, M. (2008).** Mont Terri Rock Laboratory—Project, programme 1996 to 2007 and results, no. 3. *Swiss Geological Survey, Wabern*.
- Brace, W. F. (1978).** A note on permeability changes in geologic material due to stress. *Pure and Applied Geophysics*, *116(4)*, 627-633.
- Celia, M. A., & Bachu, S. (2003, January).** Geological sequestration of CO₂: is leakage unavoidable and acceptable?. In *Greenhouse Gas Control Technologies-6th International Conference* (pp. 477-482). Pergamon.
- Chandler, M. R., Meredith, P. G., Brantut, N., & Crawford, B. R. (2016).** Fracture toughness anisotropy in shale. *Journal of Geophysical Research: Solid Earth*, *121(3)*, 1706-1729.
- Corkum, A. G., & Martin, C. D. (2007).** The mechanical behaviour of weak mudstone (Opalinus Clay) at low stresses. *International Journal of Rock Mechanics and Mining Sciences*, *44(2)*, 196-209.
- Hack, H. R. G. K., Geerts, R., Goetheer, E. L., Siedsma, J., van der Valk, B., Vogel, R. L., ... & de Zoeten, G. (2019).** Rotterdam CCUS Project (Porthos); Advies over reikwijdte en detailniveau van het milieueffectrapport.
- Harvey, O. R., Qafoku, N. P., Cantrell, K. J., Lee, G., Amonette, J. E., & Brown, C. F. (2013).** Geochemical implications of gas leakage associated with geologic CO₂ storage - A qualitative review. *Environmental science & technology*, *47(1)*, 23-36.
- Herzog, H., & Golomb, D. (2004).** Carbon capture and storage from fossil fuel use. *Encyclopedia of energy*, *1(6562)*, 277-287.
- Hou, Z., Rockhold, M. L., & Murray, C. J. (2012).** Evaluating the impact of caprock and reservoir properties on potential risk of CO₂ leakage after injection. *Environmental Earth Sciences*, *66(8)*, 2403-2415.
- ISRM (1978); Bieniawski, Z. T., & Hawkes, I. (1978).** Suggested methods for determining tensile strength of rock materials. *Int J Rock Mech Min Sci Geomech Abstr*, *15(3)*, 99-103.

- ISRM (1988); Franklin, J. A., ZONGQI, S., Atkinson, B. K., Meredith, P. C., Rummel, F., Mueller, W., ... & Bobrov, G. F. (1988).** Suggested methods for determining the fracture toughness of rock. *International Journal of Rock Mechanics and Mining & Geomechanics Abstracts*, 25(2).
- Morales, S. E., & Holben, W. E. (2014).** Simulated geologic carbon storage leak reduces bacterial richness and alters bacterial community composition in surface soil. *Soil Biology and Biochemistry*, 76, 286-296.
- Neuzil, C. E., & Tracy, J. V. (1981).** Flow through fractures. *Water Resources Research*, 17(1), 191-199.
- (Pearson et al.) Suisse. Office fédéral des eaux et de la géologie. (2003).** Mont Terri project: Geochemistry of water in the Opalinus clay formation at the Mont Terri Rock Laboratory (*Vol. 5, p. 321*). *Office fédéral des eaux et de la géologie OFEG*.
- Pyrak-Nolte, L. J., Cook, N. G., & Nolte, D. D. (1988).** Fluid percolation through single fractures. *Geophysical Research Letters*, 15(11), 1247-1250.
- Tsang, Y. W. (1984).** The effect of tortuosity on fluid flow through a single fracture. *Water Resources Research*, 20(9), 1209-1215.
- Watson, T. L., & Bachu, S. (2009).** Evaluation of the potential for gas and CO₂ leakage along wellbores. *SPE Drilling & Completion*, 24(01), 115-126.
- Wigand, M., Kaszuba, J. P., Carey, J. W., & Hollis, W. K. (2009).** Geochemical effects of CO₂ sequestration on fractured wellbore cement at the cement/caprock interface. *Chemical Geology*, 265(1-2), 122-133.
- Yong, R., Ye, J., Liang, Q. F., Huang, M., & Du, S. G. (2018).** Estimation of the joint roughness coefficient (JRC) of rock joints by vector similarity measures. *Bulletin of Engineering Geology and the Environment*, 77(2), 735-749.
- Zhang, M. (2019).** Stress-strain-sorption behaviour and permeability evolution in clay-rich rocks under CO₂ storage conditions (*Doctoral dissertation, UU Dept. of Earth Sciences*), Chapter 5, 165-201.

Appendix A

Sample (OPA_)	Intact comp.	Tensile strength / Fracture toughness	Fracture comp.	PSP exp. (load)	PSP exp. (time)	JRC data	Bedding To Fracture Angle	Mass [g]	Length [mm]	Diameter [mm]	Density [kg/m ³]	Water content [%]
V2					X		90°	55.92	49.68	24.8	2413.54	9.71
V3					X		90°	55.65	47.72	24.8	2414.13	9.73
V5						X	90°	50.24	42.95	24.8	2421.31	10.06
V12				X			90°	51.31	44.12/ 37.46*	24.81	2405.6	9.35
V14-01					X		90°	23.59	20.25	24.8	2411.28	9.60
V16-01		X					90°	31.98	27.8	24.8	2381.15	8.23
V17-01		X					90°	13.02	11.4	24.8	2364.96	7.50
V17-02		X					90°	16.13	14	24.82	2380.69	8.21
V17-03		X					90°	23.64	20.4	24.8	2399.4	9.06

*Sample fractured along bedding plane during Brazilian splitting test, so sample was shortened and parallelized in order to be able to use sample for further experiments

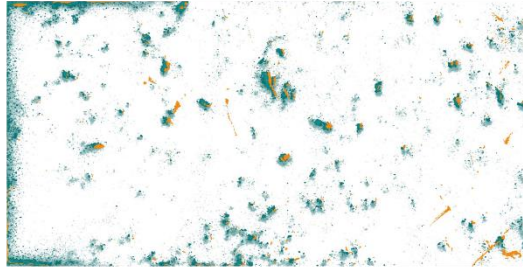
Table 1 - Information about V-series samples. What experiments are they used for and what are the dimensions and other characterizations of these samples. Intact comp. stands for intact compression, fracture comp. stand for fracture compaction. PSP exp. (load) is the experiment where stress distribution maps are made using Pressure Sensitive Paper (PSP) under different stress steps. PSP exp. (time) contains the experiments where applied stress was held constant and offset and time were the only variables. JRC data consists of the samples that were scanned at Royal Dutch Shell Amsterdam and of whom the results were used for comparison.

Sample (OPA_)	Intact comp.	Tensile strength / Fracture toughness	Fracture comp.	PSP exp. (load)	PSP exp. (time)	JRC data	Bedding To Fracture Angle	Mass [g]	Length [mm]	Average Diameter [mm]	Density [kg/m ³]	Water content [%]
H1	X			X		X	0°	57.78	49.68	24.735	2420.22	10.01
H15-1	X						-	21.20	18.46	24.715	2394.29	8.83
H20			X	X			15°	16.51	14.373	24.535	2429.49	10.43
H30-1			X	X			30°	15.45	13.372	24.655	2419.93	10.0
H30-2						X	40°	22.67	19.62	24.68	2414.96	9.77
H30-3						X	35°	22.79	19.85	24.7	2395.59	8.89
H45	X						-	22.72	19.8	24.725	2389.66	8.62
H45-2						X	20°	22.87	19.79	24.705	2410.35	9.56
H60-2				X		X	60°	22.87	19.78	24.62	2429.07	10.41
H75	X						-	19.39	15.75	24.79	2550.93	15.95
H75-3				X		X	56.3°	22.95	19.8	24.68	2422.9	10.31
H90-1	X						90°	22.44	19.45	24.64	2419.56	9.98

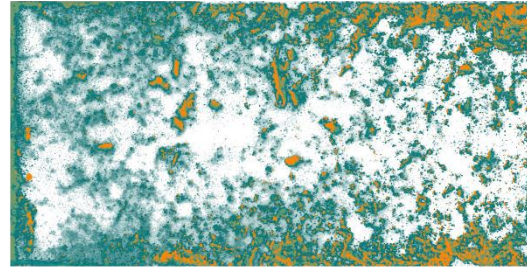
Table 2 - Information about H-series samples. What experiments are they used for and what are the dimensions and other characterizations of these samples. Intact comp. stands for intact compression, fracture comp. stand for fracture compaction. PSP exp. (load) is the experiment where stress distribution maps are made using Pressure Sensitive Paper (PSP) under different stress steps. PSP exp. (time) contains the experiments where applied stress was held constant and offset and time were the only variables. JRC data consists of the samples that were scanned at Royal Dutch Shell Amsterdam and of whom the results were used for comparison.

Appendix B

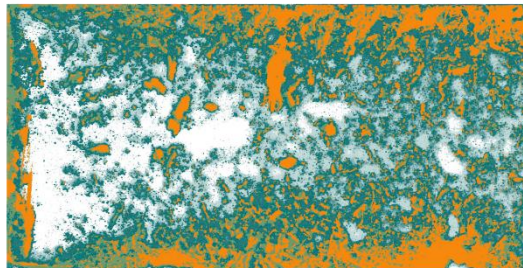
1. Sample H1



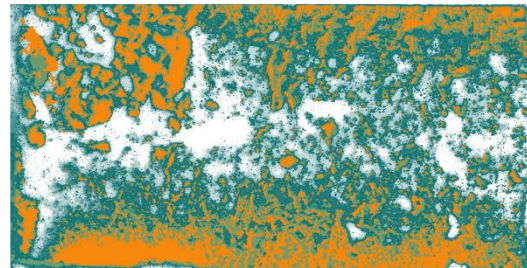
A. 0.5 MPa



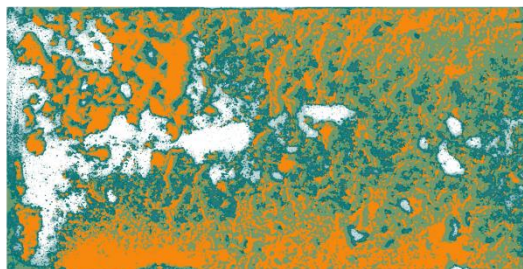
B. 3.0 MPa



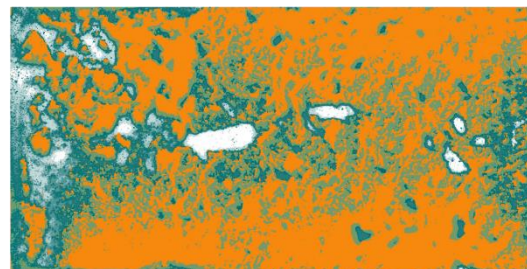
C. 5.0 MPa



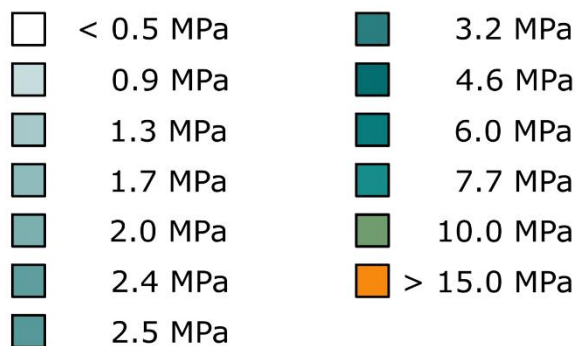
D. 7.0 MPa



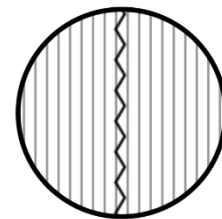
E. 10.0 MPa



F. 15.0 MPa

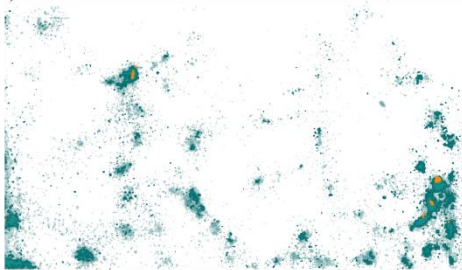



1 cm

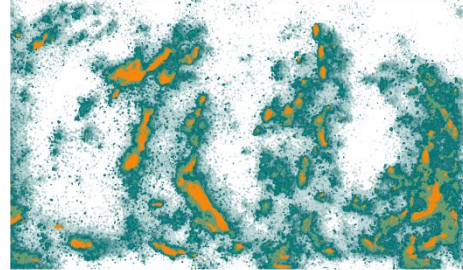


Sample H1
Angle fracture to bedding: 0°

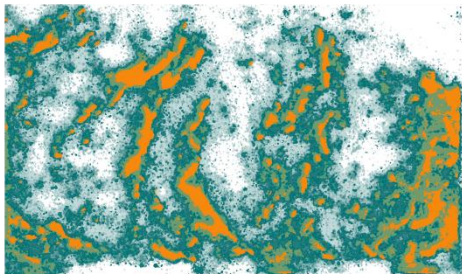
2. Sample H20



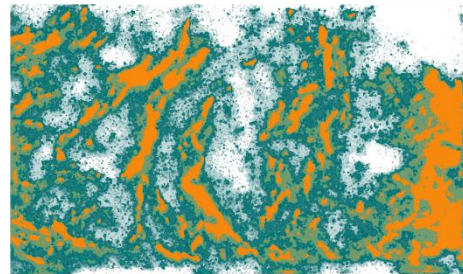
A. 0.5 MPa



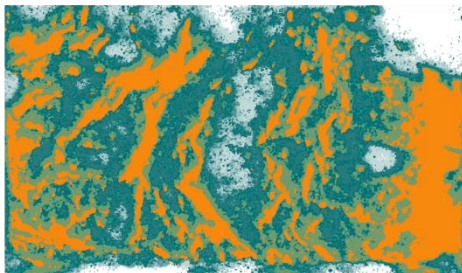
B. 3.0 MPa



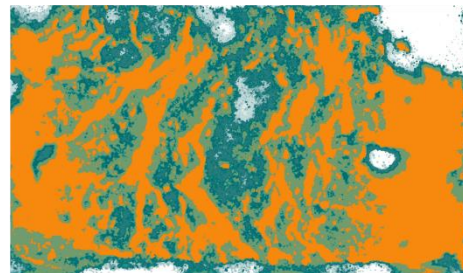
C. 5.0 MPa



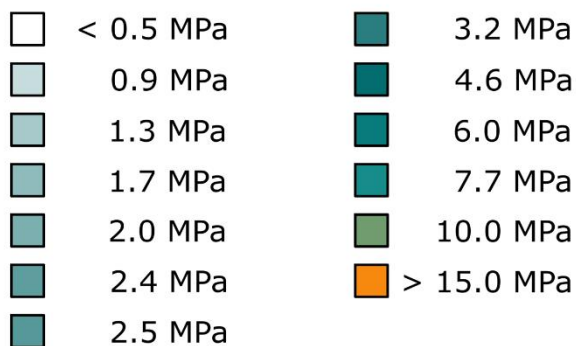
D. 7.0 MPa



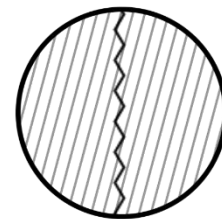
E. 10.0 MPa



F. 15.0 MPa



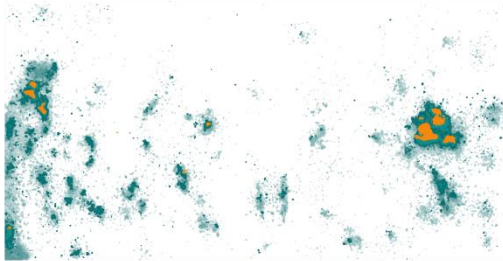
1 cm



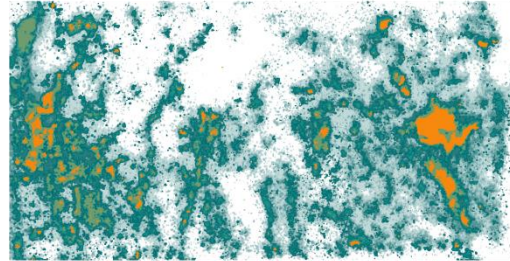
Sample H20

Angle fracture to bedding: 15°

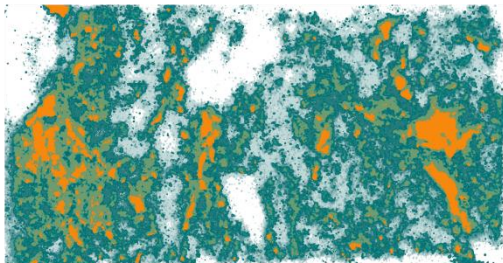
3. Sample H30-1



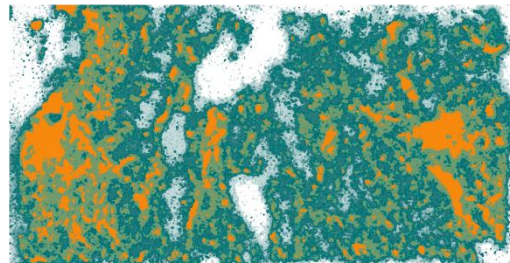
A. 0.5 MPa



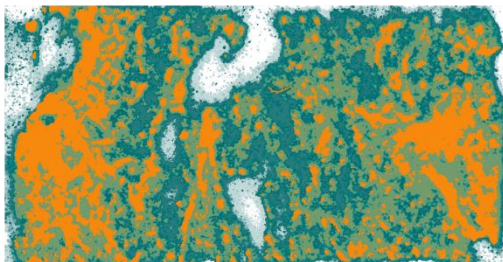
B. 3.0 MPa



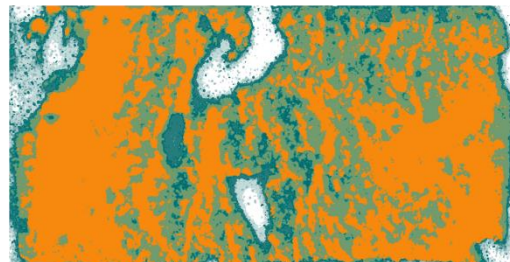
C. 5.0 MPa



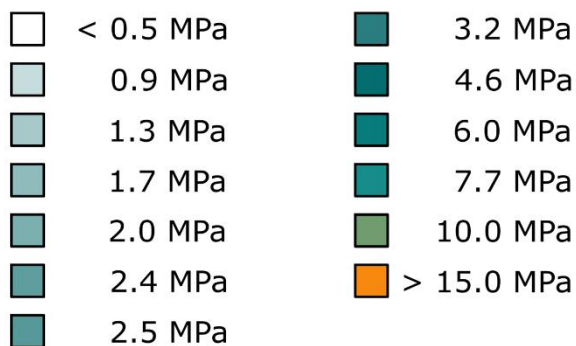
D. 7.0 MPa



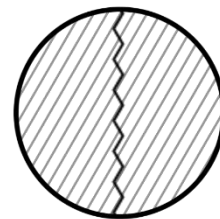
E. 10.0 MPa



F. 15.0 MPa



1 cm

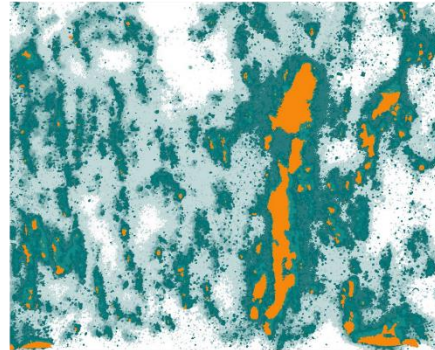


Sample H30-1
Angle fracture to bedding: 30°

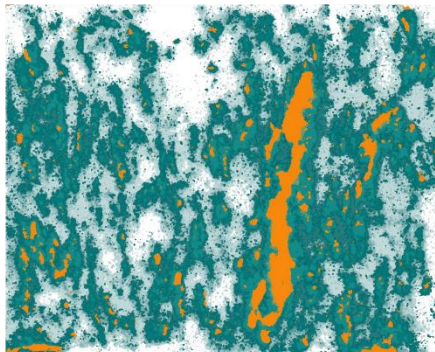
4. Sample H75-3



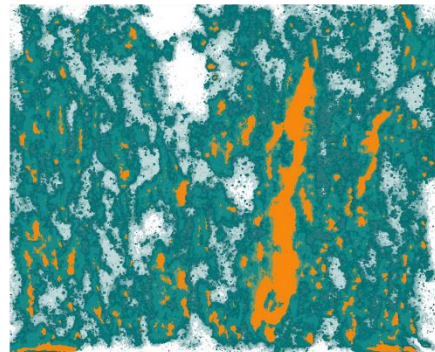
A. 0.5 MPa



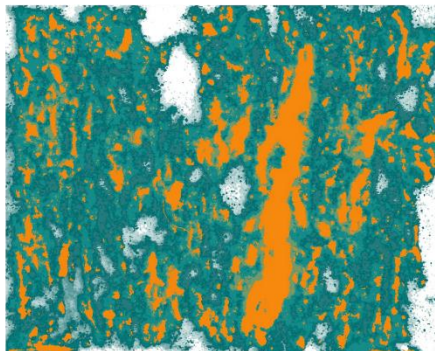
B. 3.0 MPa



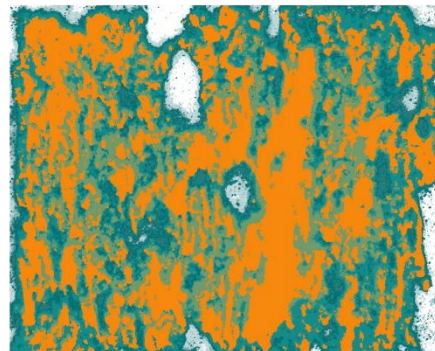
C. 5.0 MPa



D. 7.0 MPa

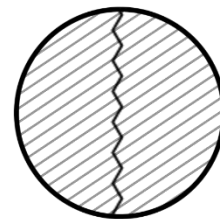
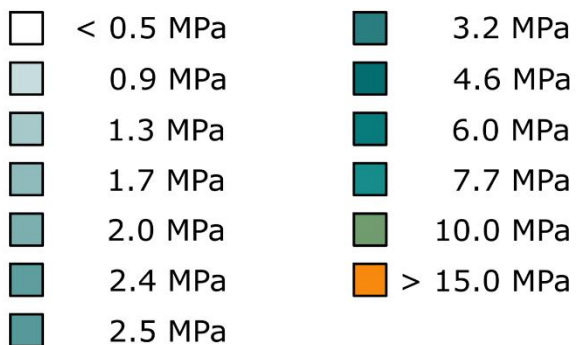


E. 10.0 MPa



F. 15.0 MPa

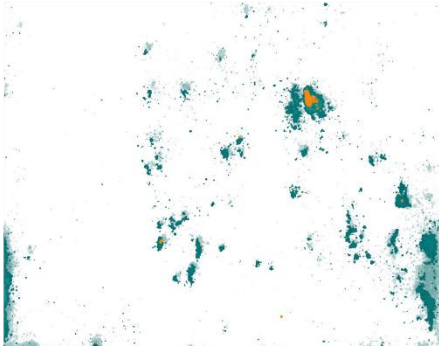
1 cm



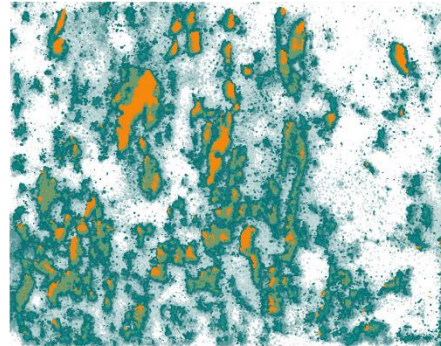
Sample H75-3

Angle fracture to bedding: 56.3°

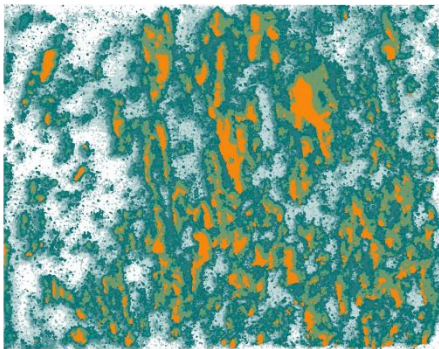
5. Sample H60-2



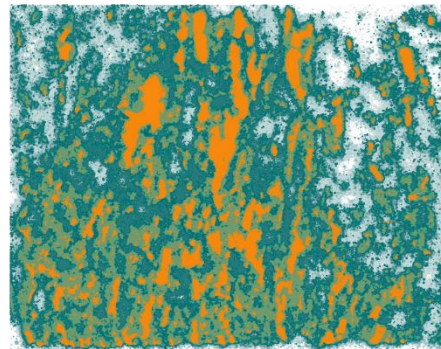
A. 0.5 MPa



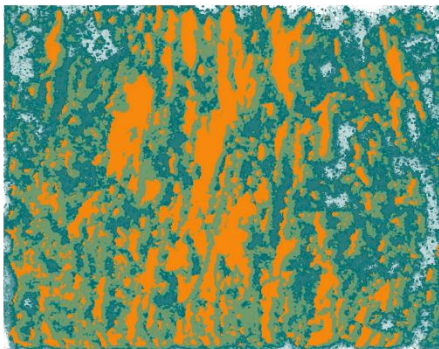
B. 3.0 MPa



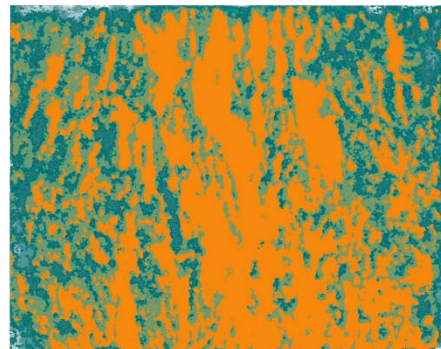
C. 5.0 MPa



D. 7.0 MPa

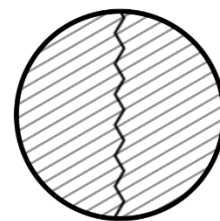
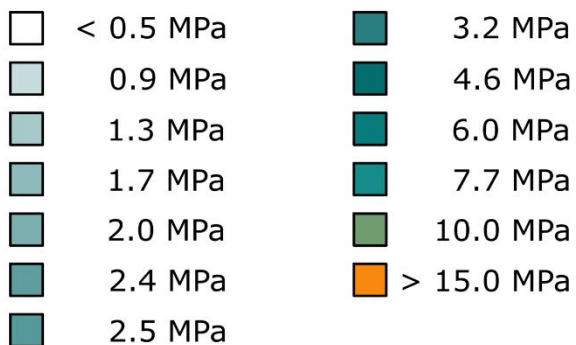


E. 10.0 MPa



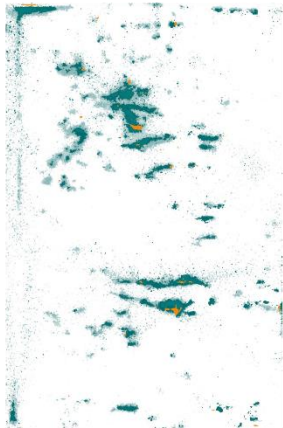
F. 15.0 MPa

1 cm

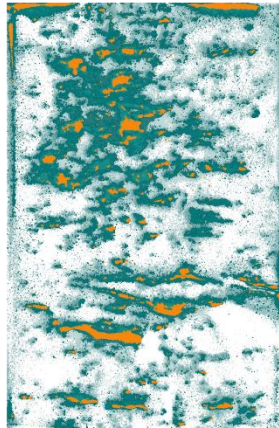


Sample H60-2
Angle fracture to bedding: 60°

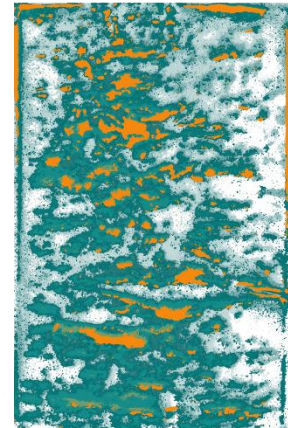
6. Sample V12



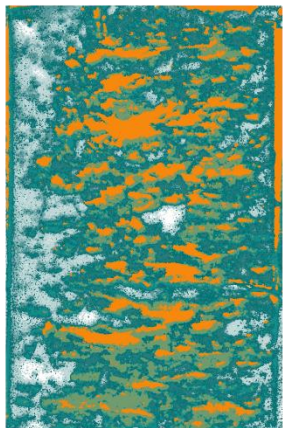
A. 0.5 MPa



B. 3.0 MPa



C. 5.0 MPa



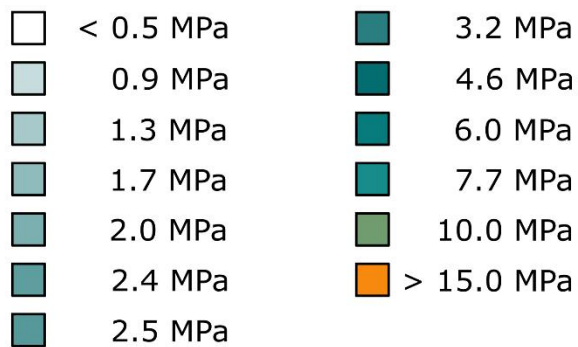
D. 7.0 MPa



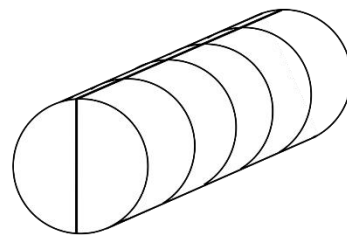
E. 10.0 MPa



F. 15.0 MPa




1 cm

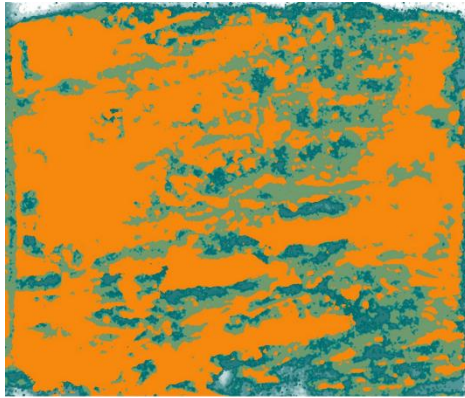


Sample V12
Fracture to bedding angle: 90°

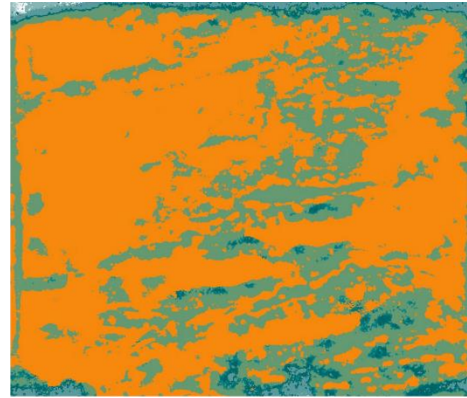
Appendix C

1. Sample V14-01:

No offset, 15 MPa applied stress



A. 0.25 hour



B. 1.25 hour



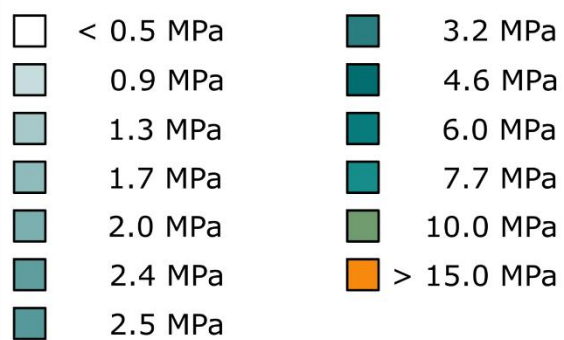
C. 5.25 hours



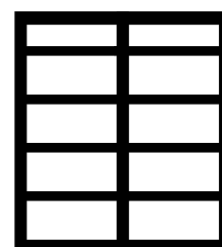
D. 21.25 hours



E. 45.25 hours

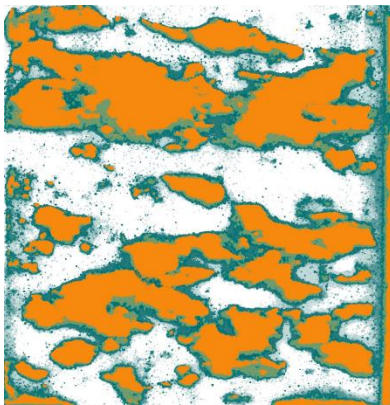



1 cm

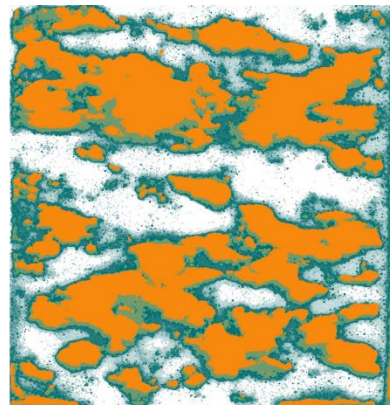


2. Sample V3:

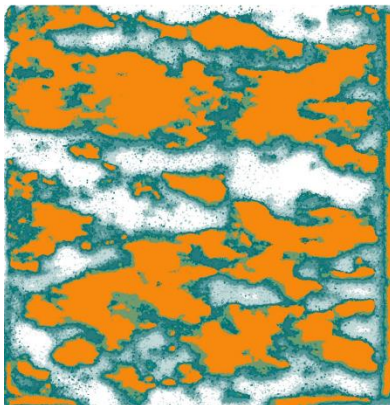
Initial dislocation of 1.5 mm, 15 MPa applied stress.



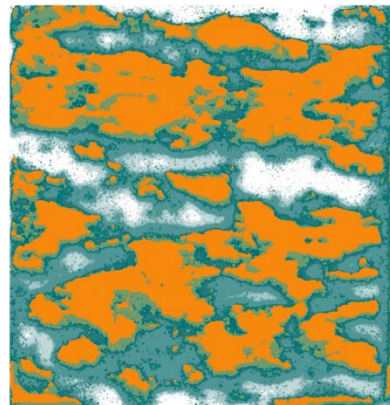
A. 0.25 hour



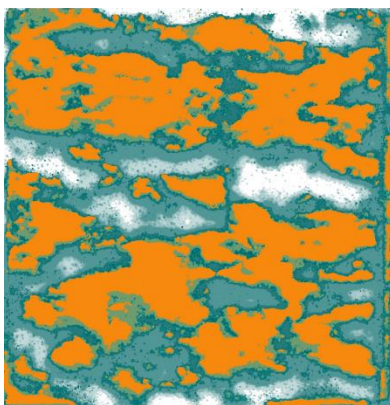
B. 1.25 hour



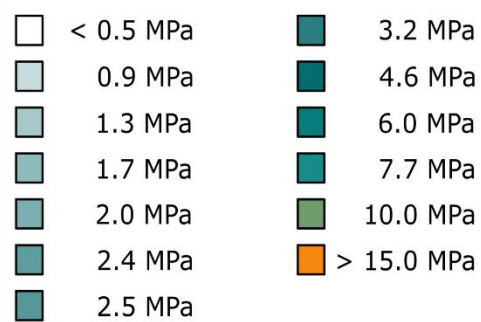
C. 5.25 hours



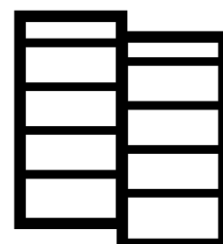
D. 21.25 hours



E. 45.25 hours

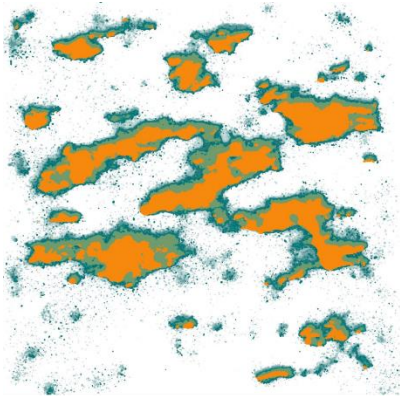


1 cm

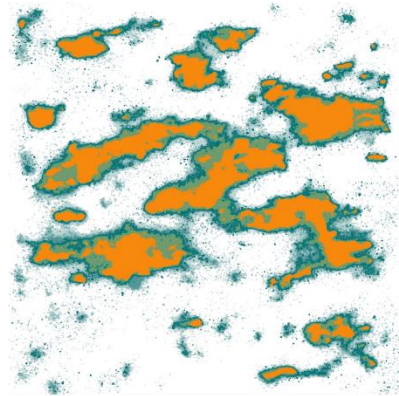


3. Sample V2:

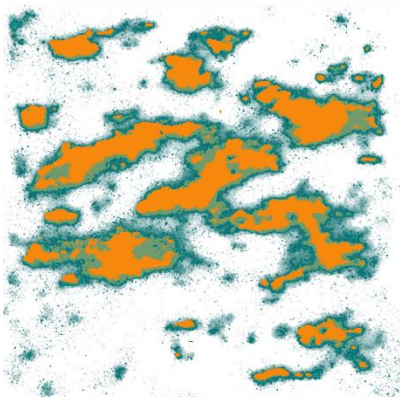
Initial dislocation of 1.5 mm, 5 MPa applied stress.



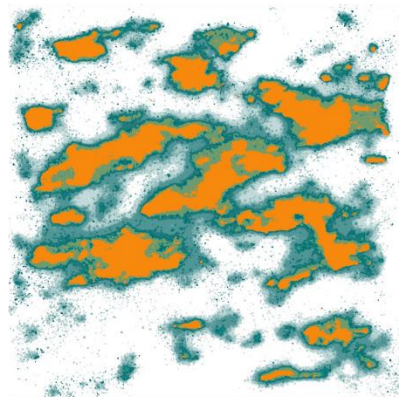
A. 0.25 hours



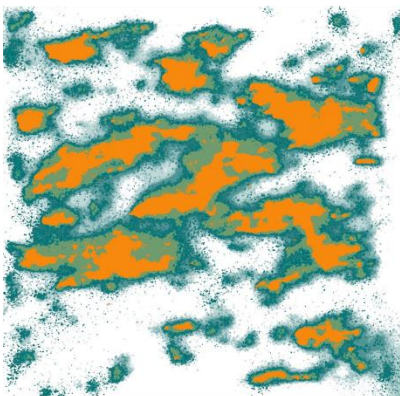
B. 1.25 hour



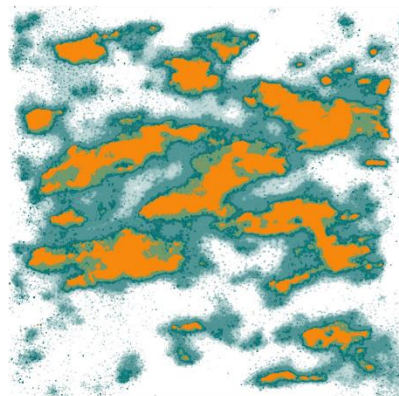
C. 5.25 hours



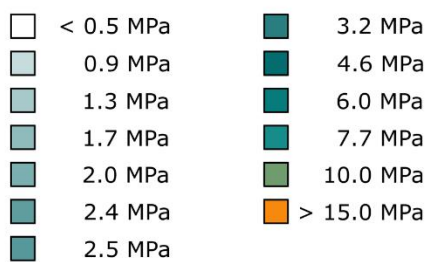
D. 21.25 hours



E. 45.25 hours



F. 113.25 hours



1 cm

